博士論文（要約）

NIR Spectrometer by a Schottky Photodetector with an Au Grating

（金回折格子を有するショットキー型光検出器による近赤外分光器）

陳　文静

博士論文

NIR Spectrometer by a Schottky Photodetector with an Au Grating

（金回折格子を有するショットキー型光検出器による

近赤外分光器）

陳　文静

Table of Contents

Chapter 1 Introduction

1.1 Near Infrared Spectroscopy

Near infrared spectroscopy (NIRS) is a spectroscopic method which employs light with wavelength range from 750 to 2500 nm to quantitatively or qualitatively analyze materials. It is based on the interaction of photons and molecules. Molecules absorb photons whose energy corresponds to their vibrational transition. The absorption of molecules in the near infrared range is mainly from the overtone and combination bands of the fundamental vibration [1]–[3].

In 1800, Frederick William Herschel first observed the infrared light with a prism and thermometers [4]. Then William de Wiveleslie Abney and Edward Robert Festing measured the infrared spectra by photographic plates in 1881 [5]. In 1905, William Weber Coblentz contributed a fundamental work for infrared spectroscopy by providing a detailed investigation on infrared spectra of plenty of materials [6]. However, because the overtones and combination in near infrared range are difficult to interpret, NIRS gained much less attention than infrared spectroscopy. In 1960s, Karl Norris, “Father of the modern near infrared spectroscopy”, measured the moisture in the soybeans and also the fat and moisture in the meat [7], [8]. His work showed the possibility of using the NIRS on quantitative analysis. The NIRS begun to attract more and more attentions.

Nowadays, NIRS as a fast, low cost, non-destructive, non-invasive and no-sample-preparation spectroscopic analysis method is widely used in many fields such as agriculture, industry quality control, food, medicine, pharmacy and so on. Various spectrums such as transmittance or diffuse reflectance spectrums are used to analyze the testing samples [1]. For example, the phytic acid (salt form: phytate) and inorganic phosphorus form the totally phosphorus in plant. The phytate strongly binds to metallic cations such as Ca, Fe, Mg and Zn, which makes these metallic cations insoluble and unabsorbable by non-ruminant animals. Reducing the phytic acid to increase the inorganic phosphorus is beneficial to the nutrition of food and the environment. S.R. Delwiche and coworkers measured the diffuse reflectance and transmittance spectrums of soybeans to analyze the inorganic phosphorus levels using NIRS [9]. In industry, NIRS is used in monitoring the concentration of monomer in the formation process of polymer [10]. NIRS is also used to analyze olive oils such as the adulteration of the oil and quality parameters like free fat acids and peroxide values of the oil [11] . Near infrared oximetry is used to measure the oxygenation values of brain and tissues based on the absorption spectrum of oxyhemoglobin and deoxygenated hemoglobin [12], [13]. NIRS is also used to analyze the pharmaceutical parameters like hardness, moisture and particle size [14].

The instruments for NIRS commonly contain a light source element, a wavelength dispersion element and a photodetection element. The latter two elements independent of the light source compose spectrometers, which are used to detect the spectrum. There are several common methods for the wavelength dispersion [1], [3]. Light emitting diodes (LEDs) which are capable of emitting specific wavelength are used as a light source element. The spectrum is measured by changing the output wavelength of the emitting diodes. The advantage of this method is low cost. However, the working wavelength range is relatively narrow. Filters such as Fabry-Perot based and Acoustic Optical Tunable Filter (AOTF) based are used to select which wavelength passes through it. However, the mirrors of the Fabry-Perot cavity need a high reflectivity and a quite good flatness. The distance between the mirrors is needed to be varied precisely to select the wavelength passing through the cavity. The main advantages of AOTF filter are having no moving part and fast speed. An acoustic wave is coupled into the crystal (such as TeO_2) through a piezoelectric transducer. The acoustic wave can periodically change the refractive index of the crystal so that the incident beam with different wavelength is diffracted into different order and hence certain wavelength can be selected. However, the material TeO_2 is toxic. Another wavelength dispersion method is using Fourier transform interferometer. This method is commonly applied to analysis materials and identify chemicals in laboratory usage. It can achieve high wavelength precision and resolution, while, the cost of Fourier transform interferometer is relatively high.

Recently, compact near infrared spectrometers are used in various fields. For example, spectrometers were used to evaluate the firmness and soluble solid content of plums during the storage period [15]. A compact near infrared spectrometer was used to classify pig carcasses fed in different ways into certain category by measuring the fat of the meat [16]. Micro-Electro-Mechanical Systems (MEMS) techniques are utilized to downscale the conventional wavelength dispersion methods including Fabry-Perot interferometer (FPI), Fourier transform interferometer, diffraction grating. Micro-spectrometers based on FP cavities formed by metal film mirrors or dielectric mirrors along with electrostatic actuators are investigated by many researches [17]–[21]. Commercial spectrometers based on FPI have also been developed. VTT Technical Research Centre of Finland Ltd presents miniature spectrometers based on MEMS FPI and piezo-actuated FPI [22], [23]. A company, Si-Ware System, provides miniature FTIR spectrometers based on MEMS actuators and mirrors [24]. Diffraction grating combined with photodetectors are used to disperse the light ever since the very beginning research of NIRS. The advantage of this method is low cost. Commercial compact spectrometers whose scales are approximately around ten centimeters are commonly based on diffraction grating and photodetectors. The different wavelengths of the incident light are diffracted to different angles by the grating and detected by the photodetectors. Concave mirrors are usually used to focus the diffracted light from the grating to the photodetectors. There is optical path between the diffraction grating and the photodetectors. The longer the optical path, the wider different wavelengths are dispersed. Hence, a higher spectral resolution can be achieved. The grating based spectrometers are relatively low cost yet with a good precision, however when they are further downscaled to be used in micro-spectrometers the tradeoff problem between the scale and the spectral resolution has to be solved due to the need of the length of the optical path [25], [26].

1.2 Schottky Photodetector

When a metal and semiconductor are intimately contacted, a potential energy barrier is formed. It was named as Schottky barrier after the contribution done by Walter Hermann Schottky. Schottky photodetector can detect near infrared light by the internal photoemission effect. When the light with energy larger than the height of Schottky barrier is incident on the metal, it will excite hot electrons to the semiconductor and produce a photocurrent. In 1931, Fowler reported the standard internal photoemission theory [27].

In near infrared range, the energy gap of silicon is larger than the energy of photons, so the common p-n junction photodetector cannot detect the near infrared light. By choosing a metal with low work function, the Schottky barrier can be very low to realize near infrared photodetection on silicon. In 1973, F. D. Shepherd, Jr. and A. C. Yang proposed silicon Schottky barrier diode arrays for infrared image [28]. According to their work, even the quantum efficiency of a Schottky barrier diode is low, the responsivity uniformity of arrays of Schottky barrier diodes is better than small band gap intrinsic semiconductor retinas. From then, the Schottky photodetector began to be used for infrared imaging [29]. The fabrication process of Schottky photodetectors is compatible with the standard large-scale integration (LSI) processing. In addition, it can realize high switching speed and uniformity in responsivity [30]. However, compared with p-n junction photodetectors, the quantum efficiency of Schottky photodetector is relatively low, which leads to the need of cooling elements to reduce the noise.

Several methods were proposed to improve the quantum efficiency of Schottky photodetectors [31]–[33]. One of these method was using a very thin film of metal, which will improve the probability of hot carriers crossing over the Schottky barrier by the multiple reflection of hot carriers to the interface of metal and semiconductor [34], [35]. Optical resonant cavity was also used to improve the quantum efficiency by increasing the light absorption [36]. Applying reverse bias to decrease the height of Schottky barrier can also improve the quantum efficiency, however the dark current also increases which causes noise for the photocurrent [31]. Waveguide metal-semiconductor-metal (MSM) photodetector with small area of metal contacted with semiconductor and asymmetry electrodes was used to achieve high responsivity under large reverse bias voltage without apparently increasing the dark current [37]. Graphene was also used to fabricate the Schottky photodetector, the two dimensional property of it can give the hot carriers more chances to have the momentum to cross over the Schottky barrier which leads to the improvement of quantum efficiency [38]. Another method is to employ surface plasmon enhancement (SPR) to increase the absorption of light. More hot electrons are generated and hence the quantum efficiency is improved. In this thesis, the SPR of an Au grating was used to couple the incident light.

1.3 Photodetection Enhanced by SPR

1.3.1 Surface Plasmon Resonance

Surface plasmon polaritons (SPPs) are electromagnetic excitations, which propagate along the interface of a dielectric and a conductor (usually metals). SPPs involve two coupled modes: the electromagnetic field in the dielectric and the oscillations of the free electrons, electron plasma, in the conductor [39], [40]. The SPR is the phenomenon of light being coupled to SPPs. Because the momentum of SPPs is larger than the incident light in free space, the SPR phenomenon only happens when the momentum of the free-space light is increased. Various methods are used to couple the free-space light to SPPs, such as prism, gratings, subwavelength holes, waveguide, and metal nanoparticles. The free electrons of metals oscillate in resonance with the electromagnetic field of light at a specific frequency. When the SPPs are confined such as in the nanoparticles, the phenomenon is called localized surface plasmon resonance (LSPR) [41]. LSPR coupling condition is related to the metal materials, size, shape and surrounding medium.

In 1902, R. W. Wood first reported the phenomenon of SPR [42], [43]. He found that under certain condition, the images of incandescent lamp from the diffraction light with certain wavelengths of a grating at certain angle were nearly black. Lord Rayleigh used the diffraction of grating to explain this interesting phenomenon [44]. However, there was a difference between the experimental results and the theoretical values using the theory. Until 1941, U. Fano proposed an explanation of "superficial waves" to supplement the Rayleigh's theory to completely describe the Wood's anomalous [45]. In 1968, A. Otto and E. Kretschmann successfully excited SPPs using a prism with two different configurations, which are known as Otto configuration and Kretschmann configuration [46], [47]. Both configurations utilized the total internal reflection to generate the evanescent wave to excite the SPPs on the interface of metal and air. In Otto configuration, there was an air gap between the prism and the metal where the SPPs was excited, while in Kretschmann configuration, a metal film was deposited on the surface of the prism and the evanescent wave passed through the metal film then excited SPPs.

The SPPs propagate along the interface of a dielectric and metal, the wave vector of SPPs relates to the permittivity of the dielectric. Therefore, the SPR coupling is very sensitive to the permittivity changes on the interface. This characteristic is widely used in SPR biosensors and chemical sensors. For example, the SPR chip can be used to detect the toxic compounds mycotoxins in food [48]. The SPR-based Biacore system is used in various bio-sensing applications such as the interaction of nucleic acid and ligand [49]. The electromagnetic field enhancement effect of LSPR is used in the surface-enhanced Raman spectroscopy [50]. The SPPs can also be used in the near-field optics such as scanning near-field optical microscope and super lens below the diffraction limit [50]. Photonic components based on SPPs such as waveguide and lasers capable of manipulating the light are useful for the future photonic integrated circuit technology [51]. The SPR and LSPR are also used to improve the quantum efficiency of photodetection.

1.3.2 **Photodetection Enhanced by SPR on Gratings**

Photodetection enhancement by SPR is mainly because of the extra light absorption when the light is coupled into SPPs. These SPPs decay and produce more hot electrons. In this way, the quantum efficiency of photodetectors is improved. Photodetection enhanced by SPR is usually realized by integrating a SPPs coupling structure with a photodetector. Schottky photodetector is preferred as the photodetector, because the metal surface of it can be easily structured (grating, holes, nanoparticles and so on) to satisfy the SPR coupling condition [52].

In 1981, A. S. Karakashian calculated the quantum efficiency of an Au/n-Si Schottky photodiode with the SPPs excited by an Otto configuration [53]. When the SPR happened, the quantum efficiency of the photodiode increased. They suggested that the Schottky photodiode could be used to observe the SPR. In 1983, J. Derov and coworkers measured the quantum efficiency of a Schottky photodiode with SPPs excited at an Otto configuration [54]. Their work showed that the SPPs could generate photocurrent in Schottky photodiode. Various SPR coupling methods are used to couple the light into SPPs to improve the quantum efficiency of photodetection such as gratings, metal nanoparticles and waveguide. [52]. In this work, an Au grating is used as the SPPs coupler.

Metal grating is a conventional way to increase the wavenumber of the light by adding extra diffraction components to the light. Because the grating is easy to fabricate, it was used to improve the absorption of light for various photodetectors. In 1982, A. M. Glass and coworkers fabricated a visible range metal-insulator-metal (MIM) detector with crossed gratings. The enhancement effect of grating was proved by comparison with a smooth substrate [55]. In 1986, K. Berthold and coworkers used sinusoidal gratings to improve the responsivity of a Metal-insulator-semiconductor (MIS) photodetector [56]. The enhanced quantum efficiency was up to 30% at the wavelength of 632.8nm. In 1985, S. R. Brueck and coworkers reported an Au-InP Schottky photodetector with gratings. The responsivity enhancement by the SPR on the Au gratings was observed over 30 times [57]. In order to solve the problem of trade-off between the response speed and quantum efficiency, the electrodes of metal-semiconductor-metal (MSM) photodetectors were patterned to subwavelength gratings, which can increase the quantum efficiency by improving the absorption of light by SPR [58]. Single or dual gratings were also used to enhance the efficiency of solar cells [59], [60].

1.4 Background and State-of-the-art

As introduced in the first section, diffraction gratings and photodetector array are widely used in compact commercial spectrometers. However, when this method is used for small-scale spectrometers like micro-spectrometers, in order to achieve high spectral resolution, a long optical path between the grating and the photodetector array is needed. As a result, the optical path limits the downscaling of this method. In order to overcome it, instead of the diffraction phenomenon, the SPR of a grating is utilized in this thesis. There is no longer an optical path between the grating and the photodetector. The light is directly coupled to SPPs and detected as a photocurrent, the whole process occurs on the surface of the grating and the Schottky junction inside the photodetector. In addition, the process of the light coupling to SPPs is intensive and produces a high signal to noise ratio (SNR) photocurrent. Therefore, using SPR to couple different wavelengths is able to achieve spectrum measurements with a high spectral resolution.

A photodetector enhanced by SPPs is wavelength-selective, which has been proved by two groups. Early in 1988, M. Jestl and coworkers presented that the detector is wavelength-selective with the light incident at certain angle and that changing the angle of incidence can vary the sensitive wavelength [61], [62]. They gave a brief suggestion that this angular wavelength-selective characteristic could be possibly used in spectrum measurement. In their work, a Schottky detector with an Ag sinusoidal grating was fabricated on an n-type GaAs substrate. The Ag sinusoidal grating worked as the SPR coupler. The Ag of the grating and the n-type GaAs formed a Schottky junction to generate photocurrent. The photocurrents of four pairs of detectors were measured by varying the wavelength of the incident light. The grating orientation of the two detectors of each pair was different to make sure that the SPR is only occurring on one detector at the same angle. During the experiment, the incident light passed through a convex lens to become divergent light. The four pairs of the detectors were tilted behind the convex lens to make the light come onto each pair at different angles. The measured photocurrent curve of each pair by varying the wavelength presented a peak at a certain wavelength, which proved the wavelength-selectivity of the detector. However, a continuous spectrum was not obtained in their work.

In 2012, Ali Sobhani and coworkers reported that a Schottky photodetector enhanced by SPPs on grating had wavelength-selectivity [63]. They proved that changing the parameters of the grating could vary the sensitive wavelength. Au grating with nano-slits was fabricated on an n-type silicon substrate. Titanium layer as an adhesion layer between the Au grating and silicon forms Schottky junction with the silicon. The light was coupled to SPPs by the LSPR of the Au grating. According to their experiment results, the responsivity of the photodetector showed a narrowband wavelength-selectivity. Photodetectors with gratings of different inter-slit distances were measured. The sensitive wavelength changed with the inter-slit distance.

In this thesis, the sensitive wavelength of a Schottky photodetector enhanced by SPR is varied by changing the angle of incidence. A rectangular Au grating was fabricated on an n-type silicon substrate to form the Schottky photodetector. The Au grating wavelength-selectively couples the light to SPPs. The Schottky junction formed by Au and n-type silicon collects the hot electrons from SPPs decay into a photocurrent. The mechanism of wavelength-selectivity of the the photodetector is the same as the previous study. However, in order to obtain a spectrum, it is not only necessary to vary the sensitive wavelength of the photodetector, but we have to separate the photocurrents of different wavelengths. Because even each photocurrent from a non-sensitive wavelength is very small, the sum of these photocurrents may produce a noise comparable with the signal of the sensentive wavelength, which could reduce the presicison of a measured spectrum.

Therefore, a matrix calculation method was proposed to separate the photocurrents of different wavelengths. The wavelength range of the spectrum was discretized into wavelength components. Responsivity is a characteristic parameter of a photodetector, which describes the efficiency of converting the power of the light to the photocurrent. The responsivities of each wavelength component at different angles of incidence were used to construct a matrix. The matrix presents the angular wavelength-selective property of the proposed detector, which can be pre-calculated. The photocurrent versus angle of incidence curve of a tested light was measured. With the pre-calculated matrix and the measured photocurrent curve, the power distribution of each wavelength of the light, the spectrum, can be obtained. Due to using the SPR of grating and the matrix calculation method, spectrum measurement with a high spectral resolution can be achieved without limitation by the length of the optical path in the conventional grating based spectrometers.

1.5 Organization of Thesis

Chapter 1 Introduction

Firstly, the potential application field of this work, near infrared spectroscopy, was briefly introduced. Then, the research backgrounds of Schottky photodetector and photodetection enhancement by SPR were presented. In the final section, the motivation and objective of this thesis were introduced. Previous studies that prove the wavelength-selectivity of Schottky photodetector enhanced by SPR were introduced in detail. The originality points of this research are realizing continuous spectrum measurement utilizing a SPR enhanced Schottky photodetector and proposing a matrix calculation method to separate the photocurrent response of wavelengths.

Chapter 2 Theory

In this chapter, the working mechanism of the proposed photodetector was introduced. The structure of the proposed photodetector was firstly introduced. Then how the SPR couples light into SPPs on a grating was introduced including the dispersion of SPPs, the SPR coupling condition of a metal grating, and the Lorentz-Drude model of permittivity of Au. Then the photodetection mechanism by the Schottky junction was presented. Finally, the mechanism of spectrum calculation using a responsivity matrix and photocurrent of the proposed photodetector was presented.

Chapter 3 Simulation and Fabrication

Firstly, Au gratings with different profile parameters including the slit height, the thickness of Au layer, the pitch and the fill factor were simulated using COMSOL Multiphysics. Then the Schottky barrier height of the photodetector was investigated by testing the I-V curve and responsivity of a fabricated Schottky photodiode. Finally, the fabrication process of the photodetector was introduced.

Chapter 4 Experiment and Results

In order to confirm the SPR can be excited on the design Au grating and detected as photocurrent, the reflectance and photocurrent of a fabricated photodetector were measured. Then the spectrum measurement experiments were introduced. The experiment steps and parameters of the tested photodetector were firstly presented. Then the experiment of measuring the responsivity matrix of the detector was introduced and the spectrums of near infrared light with narrow single wavelength and with mixed multiple wavelengths were measured by the photodetector. The results were compared with those measured by two commercial spectrometers with high spectral resolution.

Conclusion

The whole work of this thesis was summarized and the potential applications were discussed.

Chapter 2 Theory

In this chapter, the structure of the proposed photodetector is firstly introduced. Then the coupling condition and the angular wavelength dependent characteristic of surface plasmon resonance on a grating are introduced in the second section. The photodetection mechanism of the photodetector is introduced in the third section. The spectrum calculation using the photodetector is explained in the final section. The important point is the definition of a responsivity matrix, which describing the angular wavelength-selectivity of the photodetector. The responsivity matrix is used to extract the spectrum from the photocurrent of the photodetector.

2.1 Structure of Proposed Photodetector

The structure of the proposed photodetector is shown in **Figure 2.1**. A rectangular Au grating was fabricated on the surface of n-type silicon wafer. An aluminum film was deposited on the bottom of the silicon wafer. The photodetector can be seen as two parts by different functions: the Au grating for wavelength-selective light absorption and the Schottky junction for photodetection.

The wavelength-selective light absorption process is realized by surface plasmon resonance (SPR) of the Au grating. The SPR is the resonant oscillation of the surface electron of the metal facing dielectric material. The permittivity of the dielectric and the metal present positive real and complex values, respectively. In particular, it is required that the real part of the permittivity of the metal is negative to excite SPR. The incident light is coupled to surface plasmon polaritons (SPPs) under the SPR coupling condition. The SPPs decays and produces hot electrons. The Schottky junction collects the hot electrons to form the photocurrent. The SPR of an Au grating of certain wavelength occurs at a specific angle of incidence. Therefore, the photocurrent versus angle of incidence curve of the detector contains wavelength information. This is used to calculate the spectrum of the incident light.

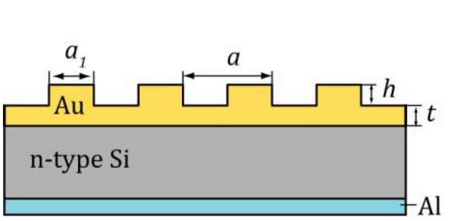

Parameters	Symbol
Pitch	a
Fill factor(a_1/a)	f
Slit height	h
Au layer thickness	t

Fig. 2.1 Structure and parameters of the proposed photodetector.

2.2 Surface Plasmon Resonance on a Grating

2.2.1 Dispersion Relation of SPPs

SPR is a phenomenon that the light is coupled to a surface wave, surface plasmon polaritons (SPPs), on a metal and a dielectric interface. The coupling condition is that the momentum of the light matches with that of SPPs. When the SPR occurs, the reflection becomes minimal due to the intensive light coupling. SPPs propagates along the interface of the dielectric and the metal. It contains the electromagnetic wave mode in the dielectric and the oscillating electrons in the metal. The oscillating electrons of SPPs propagate as a longitudinal wave in the metal. The electric field of the SPPs on the interface is strongly enhanced and decreases away from the interface [39], [64].

The dispersion relation of SPPs can be calculated using Maxwell's equations with boundary conditions. The following derivation process referred to the books written by Sir Heinz Raether and Sir Stefan A. Maier [39], [64].

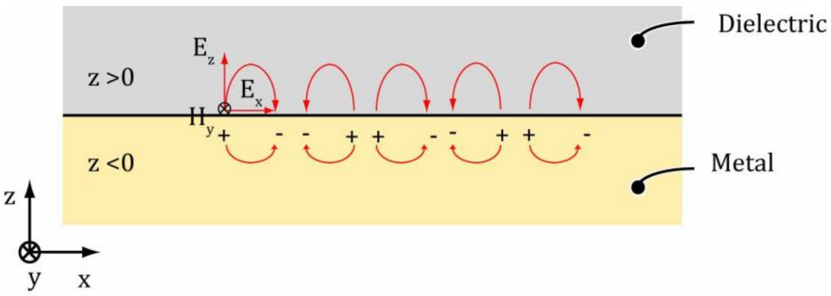

Fig. 2.2 Schematic illustration of SPPs.

The schematic illustration of SPPs is shown in **Figure 2.2**. The dielectric is set in the positive z-axis and the metal is in the negative z-axis. The electromagnetic wave mode in the dielectric and longitudinally oscillating electrons mode are coupled and propagate along the interface. The electromaganetic wave mode in the dielectric is transverse-magnetic polarized. The electric and magnetic fields in the dielectric and the metal thus can be separately described as follows

Dielectric ($z > 0$)

$$\boldsymbol{H}_d = \left(0, H_{yd}, 0\right)e^{i(k_{xd}x+k_{zd}z-\omega t)}$$

$$\boldsymbol{E}_d = (E_{xd}, 0, E_{zd})e^{i(k_{xd}x+k_{zd}z-\omega t)}$$

Metal ($z < 0$) **(2.1)**

$$\boldsymbol{H}_m = \left(0, H_{ym}, 0\right)e^{i(k_{xm}x-k_{zm}z-\omega t)}$$

$$\boldsymbol{E}_m = (E_{xm}, 0, E_{zm})e^{i(k_{xm}x-k_{zm}z-\omega t)},$$

where $\boldsymbol{H}$ is the magnetic field, $\boldsymbol{E}$ is the electric field. Symbols k_x, k_y and k_z are the components of the wave vector, ω is angular frequency. The subscripts of d and m indicate that the values belong to the dielectric and the metal, respectively.

There is no electric source at the interface. The external charge ρ and current density $\boldsymbol{J}$ are zero. The dielectric and the metal are assumed as linear, isotropic and nonmagnetic media. Substituting the equations of $\boldsymbol{D_{d,m}} = \varepsilon_0 \varepsilon_{d,m} \boldsymbol{E_{d,m}}$ and $\boldsymbol{B_{d,m}} = u_0 \boldsymbol{H_{d,m}}$ to the commonly used Maxwell's equation, the above fields obey the following equations.

$$\text{div } \boldsymbol{E}_{d,m} = 0 \ , \tag{2.2.1}$$

$$\text{div } \boldsymbol{H}_{d,m} = 0 \ , \tag{2.2.2}$$

$$\text{rot } \boldsymbol{E}_{d,m} = -\mu_0 \frac{\partial}{\partial t} \boldsymbol{H}_{d,m} \ , \tag{2.2.3}$$

$$\text{rot } \boldsymbol{H}_{d,m} = \varepsilon_0 \varepsilon_{d,m} \frac{\partial}{\partial t} \boldsymbol{E}_{d,m} \ , \tag{2.2.4}$$

where ε_m and ε_d are the relative permittivities of the metal and the dielectric medium contacting to the metal, ε_0 is the vacuum permittivity, u_0 is the vacuum permeability and ω is the angular frequency.

At the interface (z = 0), the tangential components of the electric field and the magnetic field are continuous, the following continuity relations are obtained.

$$E_{xm} = E_{xd} = E_x \ ,$$

$$H_{ym} = H_{yd} = H_y \ ,$$

$$k_{xm} = k_{xd} = k_x \ .$$

Using the above E_x, H_y and k_x instead of the corresponding electric field, maganetic field and wave vector to the field **Equation (2.1)** and substituting the magnetic field $\boldsymbol{H}_{d,m}$ and electric field $\boldsymbol{E}_{d,m}$ into the **Equation (2.2.4)**, the following results are obtained.

$$H_y k_{zd} = \ \varepsilon_0 \varepsilon_d \omega E_x \ , \tag{2.3.1}$$

$$H_y k_{zm} = - \ \varepsilon_0 \varepsilon_m \omega E_x \ , \tag{2.3.2}$$

$$H_y k_x = -\varepsilon_0 \varepsilon_d \omega E_{zd} \ , \tag{2.3.3}$$

$$H_y k_x = -\varepsilon_0 \varepsilon_m \omega E_{zm} \ . \tag{2.3.4}$$

Dividing **Equation (2.3.2)** by **Equation (2.3.1)** gives the following equation

$$\frac{k_{zd}}{\varepsilon_d} + \frac{k_{zm}}{\varepsilon_m} = 0 \ . \tag{2.4}$$

Substituting the magnetic field $\boldsymbol{H}_{d,m}$ and electric field $\boldsymbol{E}_{d,m}$ into the **Equation (2.2.3)**, the following results are obtained.

$$k_{zd} E_x - k_x E_{zd} = \ \mu_0 \omega H_y \ , \tag{2.5.1}$$

$$-k_{zm} E_x - k_x E_{zm} = \ \mu_0 \omega H_y \ . \tag{2.5.2}$$

Substituting **Equation (2.3.1)** and **(2.3.3)** to **Equation (2.5.1)**, and **Equation (2.3.2)** and **(2.3.4)** to **Equation (2.5.2)**, and combining the equation of $c = \frac{1}{\sqrt{\mu_0 \varepsilon_0}}$, the following equations are obtained.

$$k_x^2 + k_{zd}^2 = \varepsilon_d \frac{\omega^2}{c^2} \ , \tag{2.6.1}$$

$$k_x^2 + k_{zm}^2 = \varepsilon_m \frac{\omega^2}{c^2} \ . \tag{2.6.2}$$

Combing the **Equation (2.4) and (2.6)**, we can obtain the dispersion relation of SPPs by the following equations.

$$k_x = \frac{\omega}{c} \sqrt{\frac{\varepsilon_m \varepsilon_d}{\varepsilon_m + \varepsilon_d}} \ , \tag{2.7}$$

$$k_{zd} = \frac{\omega}{c}\sqrt{\frac{\varepsilon_d^2}{\varepsilon_m+\varepsilon_d}} \ , \qquad (2.8)$$

$$k_{zm} = -\frac{\omega}{c}\sqrt{\frac{\varepsilon_m^2}{\varepsilon_m+\varepsilon_d}} \ . \qquad (2.9)$$

The electric fields of SPPs are exponentially decay, the wave vector k_{zm} and k_{zd} should be imaginary numbers. Therefore, the real part of the permittivity of the dielectric and the metal should be opposite. Further more, the real part of the permittivity of the metal should be a negative number ($\mathrm{Re}(\varepsilon_m) < 0$) and the modulus of it should be larger than that of the dielectric ($|\varepsilon_m| > \varepsilon_d$). The wave vector of the SPPs (k_x) is larger than the wave vector of the light with the same angular frequency because this part of the wave vector,$\sqrt{\varepsilon_m\varepsilon_d/(\varepsilon_m + \varepsilon_d)} = \sqrt{\varepsilon_d/(1 + \varepsilon_d/\varepsilon_m)}$, is larger than 1. It is also the wave vector of the oscillating electrons in the metal. Therefore, an extra increase of the wave vector is needed for the light to excite SPPs and couple with the oscillating elections mode. Several methods are commonly used such as prisms, gratings, waveguide and nanoparticles to increase the momentum.

2.2.2 SPR Coupling Condition on a Metal Grating

The photodetector in this thesis utilizes an Au grating to match the wave vectors between the light and that of the SPPs along the interface of the grating and air. The Au grating diffracts the incident light. The wave vector of the diffracted light along a grating surface is given by the following equation

$$k_g = \frac{\omega}{c}\sqrt{\varepsilon_d}\sin\theta + \frac{2n\pi}{a} \qquad n = 0, \pm 1, \pm 2, \pm 3 \ \cdots, \qquad (2.10)$$

where ω and c are the angular frequency and the speed of the light, respectively, θ is the angle of incidence, ε_d is the permittivity of the dielectric medium contacting the metal, the dielectric medium is air in this thesis, n is the diffraction order, and a is the pitch of the grating. The diffraction orders in the opposite side of the incident light are defined as positive orders.

The SPR coupling condition on a grating surface is the wave vector matching by $k_g = \pm Re[k_x]$ with an approximation that the wave vector of SPPs along the metal grating (k_x, **Equation (2.7)**) is approximately simplified to be the same as that on a flat metal [64]. The sign convention are the '+' is for the positive diffraction orders and '−' is for the negative orders. According to the SPR coupling condition, for a grating with a fixed pitch, lights of different wavelengths are coupled at different angles of incidence at certain diffraction orders.

When the angle of incidence of the light is varied, the SPR coupling condition is satisfied at a specific angle for a metal grating. The light is intensively coupled to SPPs during the process. As a result, the reflectance of the grating decreases dramatically. On the other hand, the grating reflects most of the light without SPR occurring. Therefore, the reflectance versus angle of incidence presents a sharp dip due to SPR. Because the curve with the dip presents the property of SPR, it is called SPR curve in this thesis. The angle of incidence, where the SPR occurs, is called a SPR dip angle.

The reflectance SPR curves of 1480 nm, 1500 nm and 1520 nm of diffraction order of 1 are shown in **Figure 2.3**. As shown in the figure, the SPR dip angle of each wavelength is

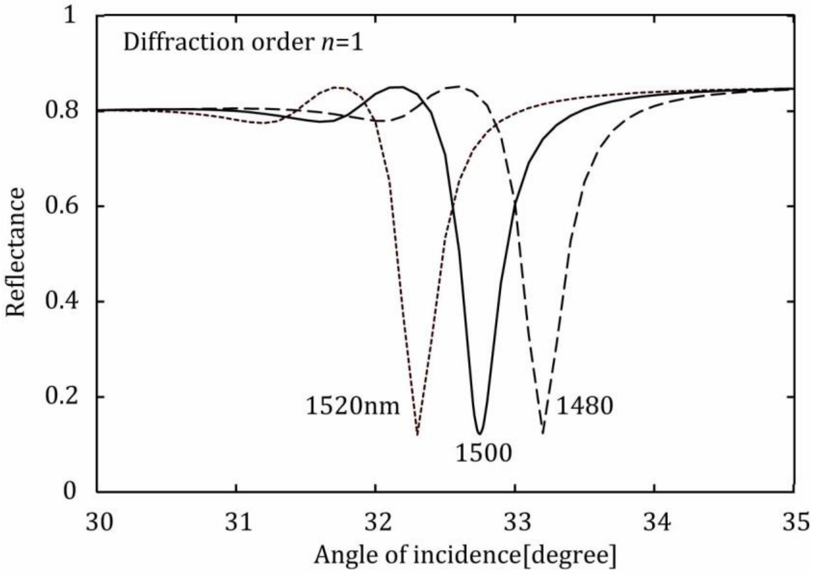

Fig. 2.3 Reflectance SPR curves of wavelengths of 1480 nm, 1500 nm and 1520 nm at diffraction order of $n = 1$.

different to each other. At SPR dip angle, only the corresponding wavelength is coupled, the other wavelengths are diffracted by the grating with a high reflectance. Therefore, the grating wavelength-selectively couples light at SPR dip angle. The SPR curve of a grating presents the SPR dip angle, which is related to a certain wavelength. Therefore, the spectrum of light can be obtained from the SPR curves.

2.2.3 Permittivity of Au

The SPR coupling condition of a metal grating contains the permittivity of Au. The permittivity of a material presents the optical properties of the material. The permittivity of metals can be described by the Drude model, which assumes the electrons in a metal as free electron gas. The motion of the electron gas is described using the kinetic theory. Several assumptions are made in Drude model. The electrons move in straight line before collisions and interact neither with each other nor with the ions. The damping is caused by a friction force that is proportional to the velocity of the electron. Drude model links the macro-optical properties of materials with the atomic structure of materials. However, in NIR range, Drude model is not sufficient to describe the permittivity of noble metals. Lorentz model takes the restoring force caused by bound-electron effect into account and adds the harmonic oscillators into Drude model. When we considered only one oscillator in the model, it is similar to the mass-spring system. The equations of motion of the two models are as follows[65], [66]

Drude model $$m\frac{d^2\vec{r}}{dt^2}+m\Gamma_0\frac{d\vec{r}}{dt}=-e\vec{E} \ , \tag{2.11}$$

Lorentz model $$m\frac{d^2\vec{r}}{dt^2}+m\Gamma_1\frac{d\vec{r}}{dt}+m{\omega_1}^2\vec{r}=-e\vec{E} \ . \tag{2.12}$$

where m is mass of electron, $\vec{r}$ is deviation of electron from its equilibrium position, $m\Gamma_{0,1}\frac{d\vec{r}}{dt}$ are the friction forces (damping force), e is the electric charge, $\vec{E}$ is the applied electric field and $m{\omega_1}^2\vec{r}$ is the restoring force which is added in Lorentz model. In the above Lorentz model, only one oscillator is considered, and ω_1 is the resonance frequency of the oscillator, however, more oscillators are usually involved in practical usage.

Substituting $\vec{E} = \vec{E}_0 \exp(-j\omega t)$ and $\vec{r} = \vec{r}_0 \exp(-j\omega t)$ into **Equations (2.11)** and **(2.12)**, the deviation of electron $\vec{r}$ can be obtained from the two equations as follows

$$\text{Drude model} \qquad \vec{r} = \frac{e\vec{E}}{m(\omega^2 + i\omega\Gamma_0)} \ , \tag{2.13}$$

$$\text{Lorentz model} \qquad \vec{r} = \frac{e\vec{E}}{m(\omega^2 + i\omega\Gamma_1 - {\omega_1}^2)} \ . \tag{2.14}$$

The deviation of electron $\vec{r}$ is also connected with the dipole moment of the electron by the equation of $\vec{p} = -e\vec{r}$. It further relates to the polarization by $\vec{P} = -Ne\vec{r}$. The polarization connects with the permittivity in Maxwell's equation as follows

$$\vec{D} = \varepsilon_0 \varepsilon_r \vec{E} = \varepsilon_0 \vec{E} + \vec{P}. \tag{2.15}$$

In this way, the permittivity (ε_r) in the two models can be obtained

$$\text{Drude model} \qquad \varepsilon_r(\omega) = 1 - \frac{{\omega_p}^2}{\omega^2 + i\omega\Gamma_0} \ , \tag{2.16}$$

$$\text{Lorentz model} \qquad \varepsilon_r(\omega) = 1 + \frac{{\omega_p}^2}{{\omega_1}^2 - \omega^2 - i\Gamma_1\omega} \ , \tag{2.17}$$

where the $\omega_p = \sqrt{\frac{Ne^2}{m\varepsilon_0}}$ is the plasma frequency, $N$is the typical electrons per unit volume, ε_0 is the vacuum permittivity and m is the mass of electron.

In this thesis, the Lorentz-Drude model combining the above two models is used to calculate the permittivity of Au. The permittivity in Lorentz-Drude model is as follows[67]

$$\varepsilon_r(\omega) = \varepsilon_r^f(\omega) + \varepsilon_r^b(\omega) \ , \tag{2.18}$$

$$\varepsilon_r^f(\omega) = 1 - \frac{{\Omega_p}^2}{\omega^2 - i\omega\Gamma_0} \ , \tag{2.19}$$

$$\varepsilon_r^b(\omega) = \sum_{j=1}^{k} \frac{f_j {\omega_p}^2}{{\omega_j}^2 - \omega^2 + i\omega\Gamma_j} \ . \tag{2.20}$$

where $\Omega_p = \sqrt{f_0}\omega_p$, f_0 is the oscillator strength and ω_p is the plasma frequency, Γ_0 is the dampling constant; k is the number of oscillators, ω_j, f_j and $1/\Gamma_j$ are the resonance frequency, strength and lifetime of *jth* oscillator. The $\varepsilon_r^f(\omega)$ represents Drude model while the $\varepsilon_r^b(\omega)$ adds the Lorentz model into the equation. The parameters of the Lorentz-Drude model refered to the paper of Alexsandar D. Rakic and coworkers[67]. The total number of the Lorentz oscillators of the data is 5. The plasma frequency of Au used in the equation is 9.03 eV. The other parameters in the model are shown in the following table.

Table 2.1 Lorentz-Drude model parameters of Au used in this thesis.

	0th(Drude)	**1st**	**2nd**	**3rd**	**4th**	**5th**
$\boldsymbol{f_j}$	0.760	0.024	0.010	0.071	0.601	4.384
$\boldsymbol{\Gamma_j}$	0.053	0.241	0.345	0.870	2.494	2.214
$\boldsymbol{\omega_j}$	0	0.415	0.830	2.969	4.304	13.32

The SPR dip angles of wavelength from 1470 nm to 1570 nm on an Au grating with pitch of 3.2 μm were calculated by **Equations (2.7, 2.10)**. The values of the calculated SPR dip angles depend on the model of the Au permittivity. In NIR range, Lorentz-Drude model is more suitable than other models such as Drude model. Therefore, the permittivity here used Lorentz-Drude model. The parameters referred to the paper of Alexsandar D. Rakic and coworkers [67]. The results are shown in **Table 2.2**. The SPR dip angle range of diffraction order −3 and 1 are approximately 8° and 3°, respectively.

Table 2.2 Calculated SPR dip angle [°] of wavelength from 1470 nm to 1570 nm of an Au grating with pitch of 3.2 μm of diffraction order n=−3 and n=1.

n\λ	1470	1480	1490	1500	1510	1520	1530	1540	1550	1560	1570
−3	21.85	22.44	23.02	23.61	24.20	24.80	25.40	26.00	26.60	27.21	27.82
1	33.13	32.91	32.69	32.48	32.25	32.04	31.83	31.61	31.40	31.18	30.97

2.3 Schottky Photodetection

The solid materials can be classified as metals, semiconductors and insulators according to the electrical conductivity. The boundary of the resistivity for metals is approximately 10^{-4} Ω-cm and that of insulators is approximately larger than 10^{8} Ω-cm [68]. The resistivity of semiconductors is between the two values. The energy band theory can describe the electrical conductivity difference of solid materials. The energy bands are collections of energy levels. As for a single isolated atom, the electrons of the atoms around the nucleus are only allowed to occupy certain energy levels. If two similar atoms are very close to each other, the energy level, which allows the electrons of single atom to occupy, will split into two energy levels. In a solid, there are plenty of atoms, so the energy level of single atom splits into numbers of energy levels. These energy levels form an energy band. The electrons of atoms fill the energy levels from the low energy levels. The valence bands are the highest energy levels that are filled with electrons at absolute zero temperature. The conduction bands are the lowest energy levels that are not completely filled by electrons. The electrons in valence bands are very hard to move by the external electric field. The electrical conductivity of a solid depends on the electrons in its conduction bands. As shown in **Figure 2.4**, the valence bands and energy bands of a metal are overlapped. The highest bands are not completely filled, thus metals have very good electrical conductivity. The energy gap of the valence bands and the conduction bands of

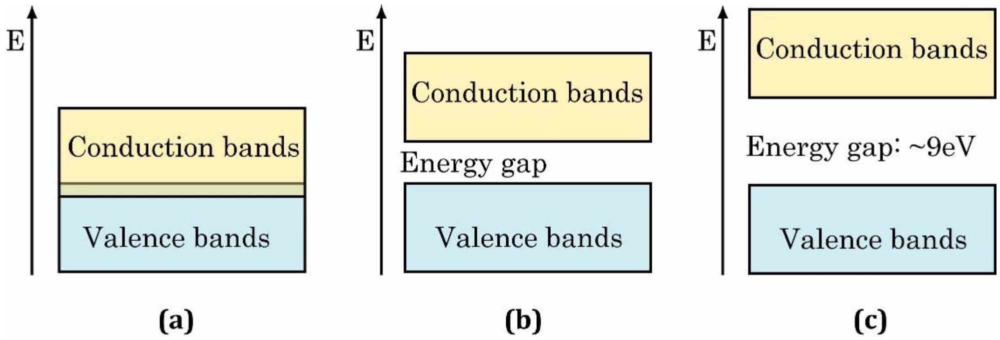

Fig. 2.4 Schematic energy bands of solid materials (a) Metals (b) Semiconductors (c) Insulators.

the semiconductors is small (silicon: ~1.12 eV, room temperature: 300 K). In room temperature, some electrons are able to be excited from the valence bands to the conduction bands, as a result the semiconductors can conduct current. The energy gap of insulator is usually defined as exceeding ~9 eV. It is very hard for the electrons in valence bands to be excited to the conduction bands, therefore the insulator have very low electrical conductivity [68], [69].

The semiconductor and the metal used for the proposed photodetector are respectively n-type silicon and Au in this thesis. Doping donor impurities to the intrinsic (purity) silicon produces the n-type silicon. The atom of the donor impurities has an extra electron that does not form a lattice bond. As a result, the electron concentration of n-type silicon is larger than that of hole. The energy band diagram of the n-type silicon and Au can be used to explain the formation of the Schottky barrier in the proposed photodetector [69].

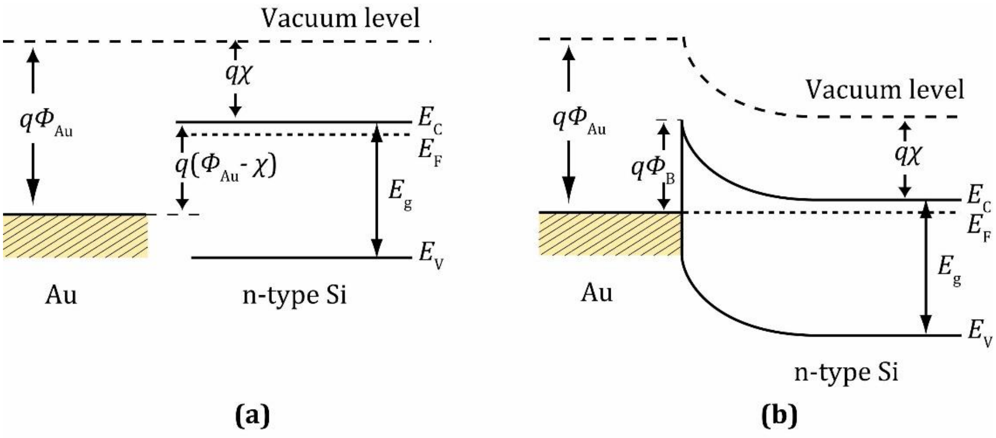

Fig. 2.5 Energy band diagram of **(a)** Isolated Au and n-type silicon **(b)** Contacted Au and n-type silicon.

As shown in **Figure 2.5 (a)**, the vacuum level is the energy level of a free electron outside of the material. The work function of Au ($q\Phi_{\mathrm{Au}}$) is the minimal thermodynamic work to move an electron out of the Au to vacuum. The electron affinity ($q\chi$) is the energy difference of the lowest energy of the conduction bands (E_{C}) and the vacuum level. The highest energy level of the valence band and the energy gap of the n-type silicon is shown as E_{V} and E_{g}, respectively. The Fermi level (E_{F}) of the isolated n-type silicon is higher than that of the Au. As shown in **Figure 2.5 (b)**, when the Au is intimately contacted with the n-type silicon, the electrons in the n-type silicon diffuse to the Au because the Fermi level of the two should be equal at a thermal equilibrium. The vacuum level must be continuous, so that the electron affinity ($q\chi$) and work function of the Au describing the property of the two materials are constant. As a result, the energy bands of the n-type silicon bend toward to the Fermi level of the Au. A potential energy barrier, Schottky barrier, is formed inside the n-type silicon. The electrons of the metal need energy larger than the Schottky barrier height to travel to the n-type silicon.

The photodetection using an Au and n-type silicon Schottky diode has two ways by the hot electrons excitation of the light with energy larger than the energy gap of silicon (~1.12 eV, room temperature) and by hot electrons generation with energy larger than the Schottky barrier height. The later usually is called as internal photoemission. The range of the wavelength used in this thesis is from 1470 nm to 1570 nm, corresponding to energy range of 0.78 eV to 0.85 eV. The energy of the photons is smaller than the energy gap of silicon and larger than the Schottky barrier height (~0.78 eV). Therefore, the photodetection mechanism of the proposed photodetector is based on the internal photoemission.

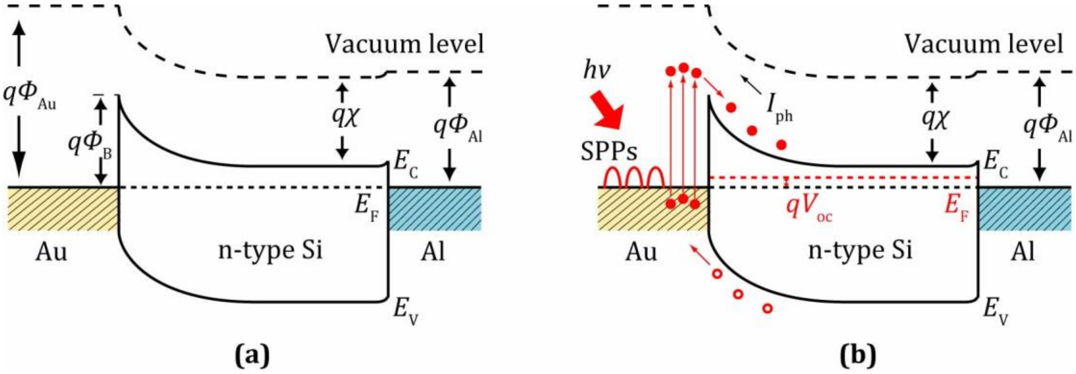

Fig. 2.6 (a) Energy band diagram of the proposed photodetector in dark condition and **(b)** with light incident.

The sources of hot electrons generation of the proposed photodetector are the SPPs decay and the directly excitation by the NIR light. The former is the dominant mechanism.

The band diagram of the detector is shown in **Figure 2.6 (a).** The Schottky barrier is formed by Au and n-type silicon. An aluminum film forms an ohmic contact with n-type silicon. As shown in **Figure 2.6 (b)**, when the light is incident on the photodetector at a SPR dip angle, the light is coupled to SPPs. Hot electrons are generated by the SPPs decay. The hot electrons with energy larger than the barrier height cross the Schottky barrier and produce a photocurrent.

The responsivity (R) is characteristic parameter of a photodetector that describes the efficiency of changing the light into photocurrent. It depends on the light absorption efficiency and internal quantum efficiency, and can be measured by the power of the incident light (P_{in}) and the photocurrent (I_{ph}) generated by the light [32].

$$R = \frac{I_{ph}}{P_{in}} \tag{2.21}$$

2.4 Spectrum Calculation

The spectrum detection of the proposed photodetector is based on the wavelength-selective absorption of Au grating at a SPR dip angle. Spectrum is calculated from the photocurrent versus angle of incidence curve of the detector. The following variables are defined to show the calculation process.

出版予定のため非公開

出版予定のため非公開

出版予定のため非公開

The spectrum is calculable using the above equation only when the responsivity matrix ***R*** is invertible. This condition is satisfied because of the wavelength-selective characteristic at SPR dip angles of the photodetector. The responsivity curves of three wavelengths and the corresponding responsivity matrix as an example are shown in **Figure 2.7**. The diagonal entries are the responsivities enhanced by SPR. They are larger than the entries in the same row and column, which makes the responsivity matrix invertible.

出版予定のため非公開

Fig. 2.7 Responsivity curves of 1463 nm, 1500 nm, 1520 nm and the responsivity matrix

出版予定のため非公開

2.5 Summary

In this chapter, the structure of the photodetector, n-type silicon wafer with rectangular grating on its surface, was firstly introduced. Then an analyzed model for the dispersion relation of SPPs and the SPR coupling condition of a metal grating were presented. The SPPs is a surface wave propagating along the interface of a dielectric and a metal. It is composed of the electric magnetic wave mode in the dielectric and the oscillation of free electrons in the metal. The SPR occurs when the momentum of the light is matching with that of the SPPs. When the parameters of the grating are fixed, SPR on a grating depends on the angle of incidence and the wavelength of the light. This makes the photodetector has the wavelength-selective light absorption property and can detect the spectrum. Then, the photodetection mechanism of the detector was introduced. The photodetection is based on the internal photoemission of the Schottky junction formed by Au and n-type silicon. The spectrum calculation process was introduced in the last section. Spectrum is obtained by a matrix calculation method using the responsivity matrix and photocurrents at SPR dip angles.

Chapter 3 Simulation and Fabrication

The discussions on parameters of the proposed photodetector and its fabrication process are introduced in this chapter. Firstly, the SPR of the Au grating is simulated using COMSOL Multiphysics. The reflectance and electric field distribution varying angle of incidence are observed. The simulation investigates the parameters of the grating including the slit height, the Au layer thickness, the pitch and the fill factor. Then the Schottky barrier height formed by Au and n-type silicon is calculated from the IV curve of a fabricated Schottky photodiode with Au film on the n-type silicon wafer. Finally, the fabrication process of the photodetector is introduced.

3.1 COMSOL Simulation of SPR on an Au Grating

3.1.1 Simulation Settings

COMSOL Multiphysics is a software environment based on finite element method (FEM). It is commonly used in various fields such as fluid, mechanical, chemical, electrical and so on. The simulation domain is divided into numerous of smaller domains called finite elements. A set of equations approximating to the original problem are used to model these elements, then all of the element equations are collected to find an approximation solution to the original problem. There are various module products available in COMSOL Multiphysics for different fields. In order to simulate the SPR phenomenon of the Au grating, RF module is used in this thesis. The physics interface of Electromagnetic Waves, Frequency Domain is used in the simulation. The Au grating structure is built in 3 dimensions (3D).

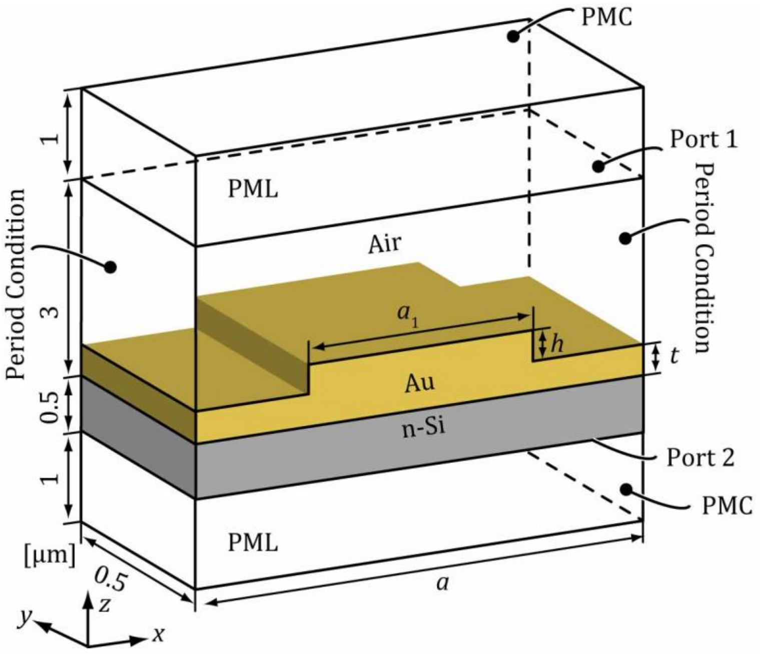

Symbol	Parameter
a	Pitch
f	Fill factor a_1/a
h	Grating slit height
t	Au layer thickness

Fig. 3.1 Geometry of the Au grating in the simulation in COMSOL Multiphysics.

The geometry information in the simulation is shown in **Figure 3.1**. One period of Au grating with silicon under it was built in the simulation domain. The parameters of the Au grating including the pitch, the fill factor, the grating slit height and the Au layer thickness were defined. Because the thickness of the n-type silicon of the photodetector is very large (~500 μm) compared to that of the Au grating (~100 nm) and SPR occurs on the surface of the Au grating, the thickness of the silicon is assumed without significant effects on the result of the simulation and is set to be 0.5 μm in the simulation. The whole Au grating is put in the air with refractive index of 1. The height (along the z-axis) of the whole simulation area is 5.5 μm. The depth (along the y-axis) of the simulation area is 0.5 μm. The width is the same as the pitch of the Au grating.

Before the simulation, the boundary conditions of the whole domain were set. As shown in **Figure 3.1**, there is only one period of the Au grating in the domain, therefore in order to describe the periodicity of the grating, which is assumed to be infinite in *x*-axis, Floquet boundary conditions were used for the left and right surfaces of the whole domain. The front and back surfaces were set to be perfect magnetic conductor (PMC) to eliminate the reflection of magnetic field from these two surfaces. The top and bottom domains were defined to be perfect match layers (PMLs). The PMLs eliminate the effects from the ports and the higher diffraction order modes of the grating. The interior of PMLs were set to be port boundary condition as Port1 and Port2 to calculate the reflectance. The option in the setting of the port property, slit condition on interior port, was active [70]. Transverse magnetic polarized plane wave was excited from the Port1 and incident on the surface of the Au grating. The setting parameters of the two ports are shown in **Table 3.1 (a)**. The angle of incidence is defined as alpha which was swept in the simulation. The refraction angle is therefore to be n_air × sin(alpha)/n_si using Snell's law, where n_air and n_si are the refractive index of air and silicon respectively. The definition of propagation constant of the incident wave and the refracted wave are shown in **Table 3.1(b)**.

Table 3.1 (a) Port property setting.

	Wave excitation	**Power**	**Magnetic field**	**Propagation constant**
Port1	on	1[W]	(0,exp(-i*kax*x),0)	abs(kaz)
Port2	off	-	(0,exp(-i*kbx*x),0)	abs(kbz)

(b) Propagation constant definition.

	Propagation constant
Air	ka=n_air*emw.k0
n-Si	kb=n_si*emw.k0
Incident wave	(kax=ka*sin(alpha), kay=0, kaz =ka*cos(alpha))
Refracted wave	(kbx =kb*sin(beta), kby=0, kbz=kb*cos(beta))

The properties of the materials were also defined. Two important parameters, the refractive index of silicon and the permittivity of Au, which change with the wavelength of the incident wave, are defined by importing data and using the interpolation of

COMSOL to get their functions instead of using the data from the material library. The data of the refractive index of silicon used in the simulation are shown in **Figure 3.2 (a)**. The data are from a website named luxpop [71], which referred to the book edited by Edward D. Palik[72]. The range of wavelength shown here is from 1 μm to 10 μm, which covers the NIR range.

(a) Refractive index of silicon

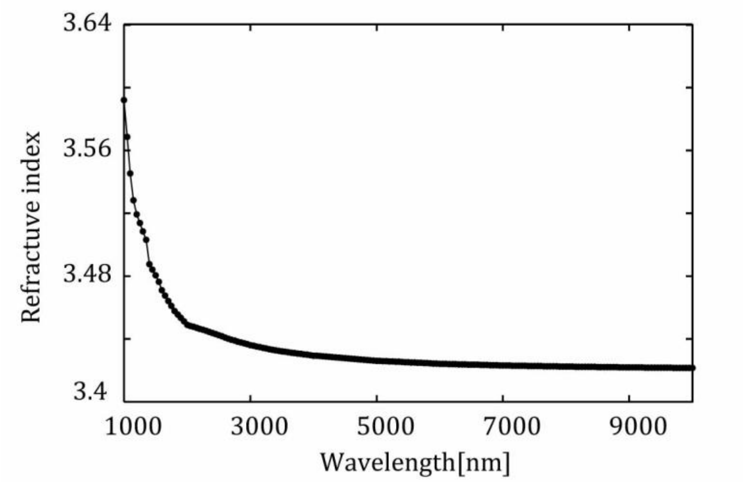

(b) Real and imaginary parts of permittivity of Au

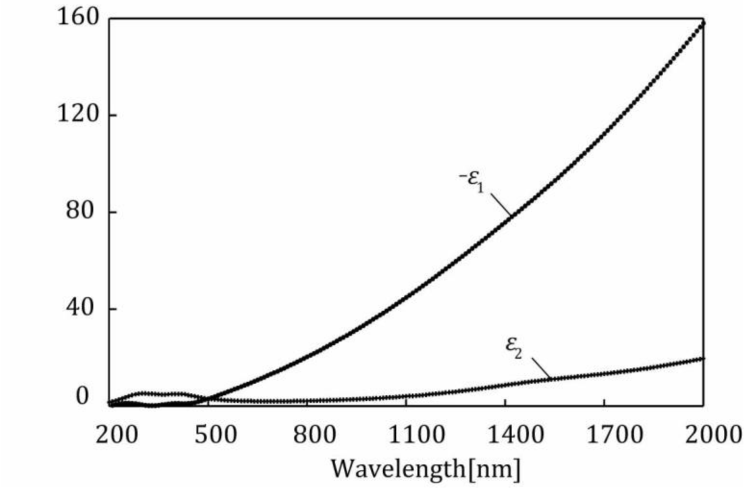

Fig. 3.2 (a) Refractive index of silicon **(b)** Real part ε_1 and imaginary part ε_2 of permittivity of Au in Lorentz-Drude model.

The permittivity of Au in the simulation used the Lorentz-Drude model with the same parameters referring the work of Alexsandar D. Rakic and coworkers [67], which was also used in Chapter 2 to calculate the SPR dip angles. It is written with the real and imaginary parts separately as $\varepsilon_{Au}(\lambda) = \varepsilon_1(\lambda) - i\varepsilon_2(\lambda)$. The value of the two parts are shown in **Figure 3.2 (b)**. As shown in the figure, Au in NIR range has a negative real part of permittivity, which allows the existence of SPPs as we discussed in Chapter 2.

3.1.2 Simulation Results

Reflectance and Electric Field of SPR

In order to confirm the light coupling and electric field enhancement by SPR, the light with wavelength of 1500 nm incident on the Au grating was simulated. The parameters of the grating were pitch of 3.2 µm, fill factor of 0.5, slit height of 100 nm and Au layer thickness of 100 nm. The reflectance and maximal amplitude of electric field on the surface of the Au grating were calculated from the simulation results. With setting the port boundary condition, the reflectance on the grating surface can be calculated from the scattering parameters (S-parameters) of ports. The calculation equation is as follows $|(\mathrm{emw.S11})^{\wedge}2|$ in COMSOL. The S11 is defined in COMSOL as the voltage reflection coefficient at Port1. The reflectance only contains the zero order of the diffraction or reflection from the grating. The amplitude of electric field was obtained by the expression $\mathrm{emw.NormE}$. The SPR will occur at angle of incidence of 23.61° corresponding to the diffraction order of -3 according to the calculation in Chapter 2. Therefore, the angle of incidence was varied from 20° to 28° in the simulation.

The simulation results are shown in **Figure 3.3**. The reflectance curve has a sharp dip at angle of incidence of 23.35°, while maximal amplitude of electric field on the surface of the Au grating (Max.Norm.E) presents a peak at the same angle. This coincides with the phenomenon of SPR. The reflectance at angles of incidence without SPR occurring is very large with a value around 0.8. It is because the Au grating reflects most of the light. However, at the angle of incidence of 23.35°, the SPR coupling condition is satisfied, the light is intensively coupled into SPPs. As a result, the reflectance becomes minimal and the electric field on the surface of the Au grating increases dramatically due to the coupling.

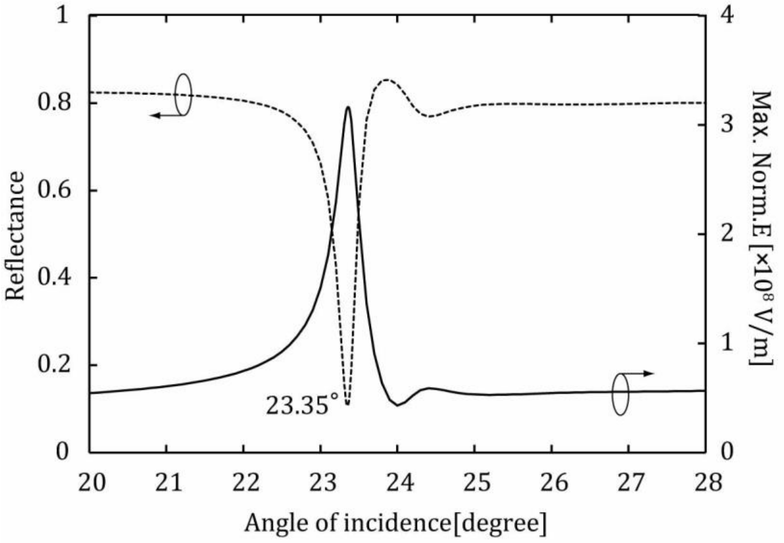

Fig. 3.3 Reflectance and maximal amplitude of $\boldsymbol{E}$ at the surface of the Au grating.

The simulated electric field without and with SPR occurring are compared in **Figure 3.4**. The angles of incidence are 20° and 23.35° respectively. The distribution of the electric field is shown in arrows and the *z*-component of it is in colors. As shown in the figure, at angle of 20°, the incident light is diffracted by the grating and forms interference patterns. The maximal amplitude of the electric field is approximately ten times smaller. On the other hand, at angle of 23.35°, the interference patterns disappear and a surface wave, the SPPs, is excited on the surface. The electric distribution of the wave is similar to that on a flat metal surface. The electric field on the side of the air is strongly enhanced. The amplitude of it is largest on the interface of the grating and air and decreases along *z*-axis departing away from the Au grating surface. The electric distribution of the SPPs on the grating proves the approximation that was made in Chapter 2 to calculate the SPR coupling condition on a metal grating and a dielectric interface is acceptable. The dispersion relation of SPPs on the interface of a flat metal with dielectric can also be approximately used on a metal grating. However, the grating profile parameters do affect the property of the SPR coupling conditions and the propagation of the SPPs, which we will discuss latterly based on the simulation.

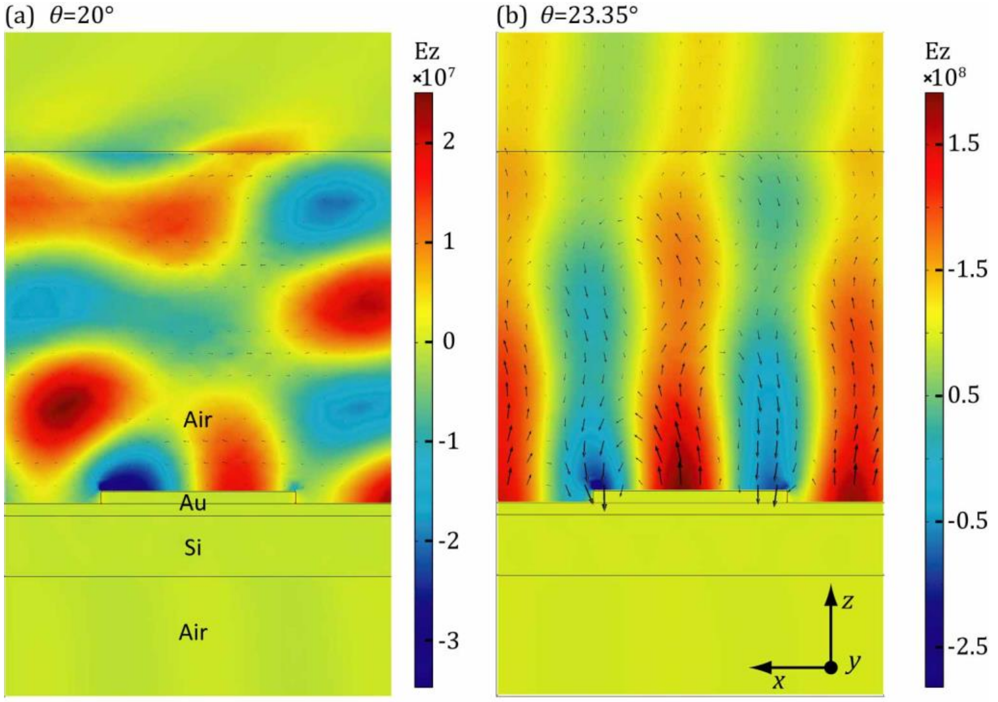

Fig. 3.4 Electric field distribution at **(a)** angle of incidence of 20° without SPR and **(b)** angle of incidence of 23.35° with SPR occurring.

The light of wavelengths of 1480 nm, 1520 nm, 1550 nm and 1560 nm were also simulated. The calculated reflectance curves are shown in **Figure 3.5**. As the wavelength increasing, the SPR occurs in larger angle. This is because the SPR is excited by diffracted light of the negative order of -3. The wave number of the SPPs is smaller in longer wavelength and it equals to the wave number of x-component of the diffracted light ($k_g = \frac{\omega}{c}\sqrt{\varepsilon_d}\sin\theta + \frac{2n\pi}{a}$). Because the diffraction order is negative, the angle of incidence is needed to be increased to provide a larger x-component. The simulated SPR dip angles are compared with those calculated by the equations in Chapter 2. The results are shown in **Table 3.2**.

The simulated values are approximately 0.3°~0.6° smaller than the calculated ones.

Table 3.2 SPR dip angle of wavelength from 1480 nm to 1560 nm.

Wavelength[nm]	**1480**	**1500**	**1520**	**1550**	**1560**
Simulated value	22.17°	23.35°	24.55	26.37°	26.98°
Calculated value	22.44°	23.61°	24.8°	26.9°	27.61

The difference is due to the approximation that the propagation constant of SPPs on grating is the same as the flat metal.

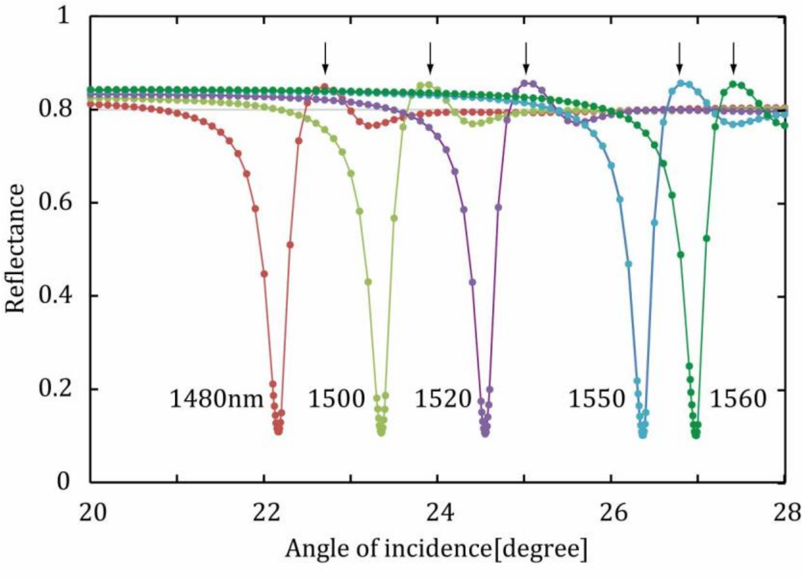

Fig. 3.5 Reflectance curves of wavelength of 1480, 1500, 1520, 1550 and 1560 nm.

There is a small peak near the SPR dip in each SPR curve that is marked with arrow in **Figure 3.5**. The reason is because the angle of diffraction of order -3 becomes 90° and its disappearance produces the increase of reflection [64]. The illustration of the diffraction of a grating is shown in **Figure 3.6**.

The condition of positive interference is that the optical path length difference (CD-AB in the figure) is the integer times of the wavelength as the following equation

$$-a\sin\theta_n - a\sin\theta = n\lambda, \tag{3.1}$$

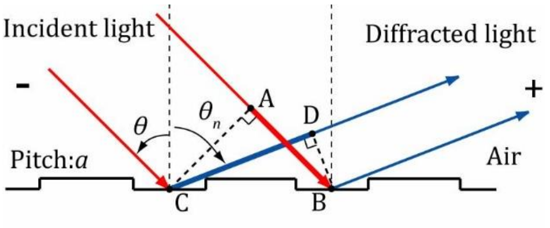

Fig. 3.6 Diffraction of a grating.

where the refractive index of air is 1, a is the pitch of the grating, θ and θ_n are the angle of incidence and the angle of diffraction of order n respectively. The pitch of the grating in simulation is 3.2 µm and the diffraction order is -3. The sign convention of the angle and the diffraction order are the same as those used in the calculation of SPR coupling condition. Angle with the anti-clockwise from the grating normal to the surface is a positive angle and the order in the opposite side from the incident is a positive diffraction order. Using the above equation with θ_n of 90°, the calculated angle of incidence of the 5 wavelengths are approximately consistent with the simulated values, the two values are shown in **Table 3.3**.

Table 3.3 Angle of incidence when angle of diffraction is 90° of order -3.

Wavelength[nm]	**1480**	**1500**	**1520**	**1550**	**1560**
Simulated value	22.7°	23.9°	25°	26.8°	27.5°
Calculated value	22.7°	23.9°	25.15°	26.9°	27.5°

Grating Slit Height

The Au gratings with different slit heights were simulated. The calculated reflectance curves are shown in **Figure 3.7**. The incident wavelength, the pitch, the Au layer thickness and the fill factor of the grating are 1500 nm, 3.2 µm, 100 nm and 0.5 respectively. The grating slit height was changed from 60 nm to 220 nm. As shown in the figure, as the height increasing, the SPR dip angle shifts to the smaller angle, the reflectance at SPR dip angle decreases and the FWHM of the SPR dip increases. According to previous work[73], [74], the propagation length of SPPs decrease lead to a larger FWHM. Because the propagation length relates to the permittivity of the metal of SPR occurring, changing the metal of the grating for example aluminum may lead to a sharper SPR dip [75]. As shown with an arrow in the figure, the angle of incidence, where the diffraction order of −3 disappears almost remains the same value. The reflectance without SPR occurring becomes smaller because of the increase of diffraction efficiency of high orders. Higher light coupling efficiency produces a larger photocurrent. Therefore, smaller reflectance at SPR dip angle is preferred for the quantum efficiency of the photodetection. However, in order to achieve high spectral resolution, sharper SPR dip with small FWHM is necessary. There is a tradeoff between the two when we design the grating slit height. For the simulated grating, 80 nm to 100 nm is an appropriate range.

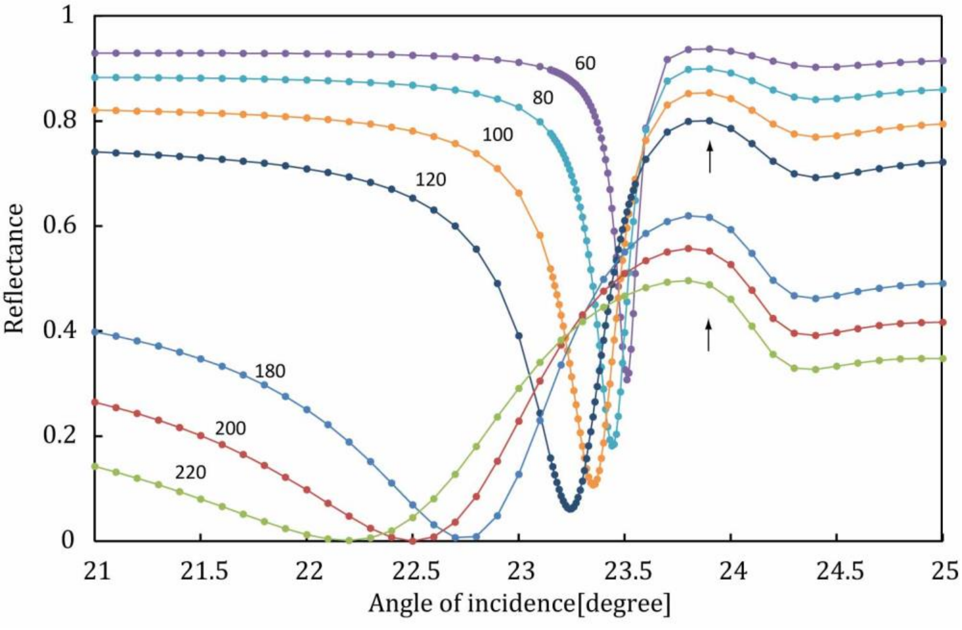

Figure 3.7 Simulated reflectance curves of grating slit height from 60 nm to 220 nm.

Au Layer Thickness

The Au gratings with different thickness of the Au layer were also simulated. The obtained reflectance curves are shown in **Figure 3.8**. The thickness of the Au layer was changed from 100 nm to 10 nm. In the range of 100 nm to 60 nm, the SPR dip shifts slightly to the left with almost the same FWHM. It suggests that for the designed grating, when the Au layer thickness is thick, the value of it has small effects on the SPR coupling condition and the dispersion relation of the SPPs. However, as the thickness further decreases from 40 nm, the SPR dip angle becomes sensitive to the thickness changing and shifts to small angle direction. The SPR dip becomes wider and shallow. The FWHM of the SPR dip is considerly larger. The reflectance at the SPR dip angle increases. The reflectance at angles without SPR occurring decreases.

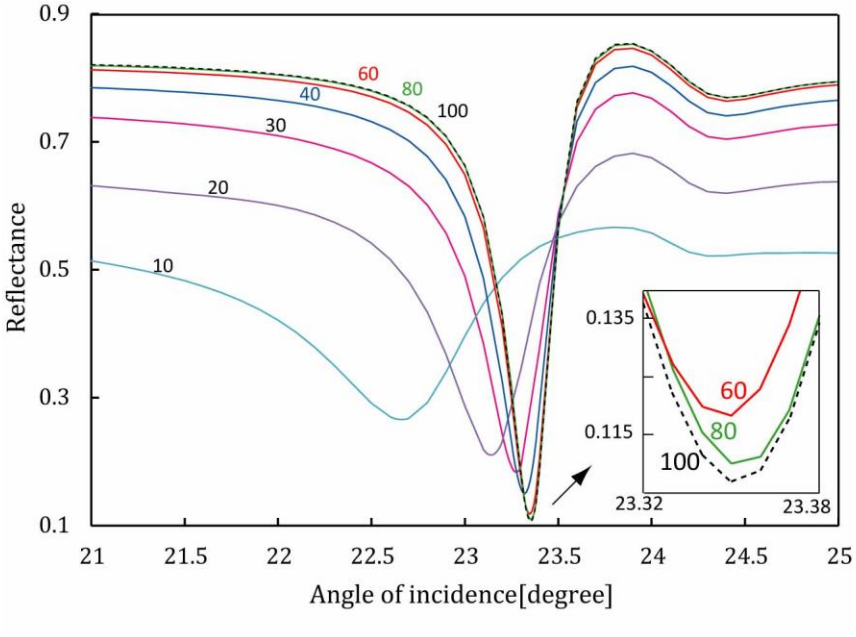

Figure 3.8 Simulated reflectance curves of Au layer thickness from 100 nm to 10 nm.

The electric field of z-component of Au layer thickness of 30 nm and 10 nm are shown in **Figure 3.9**. The angle of incidence is 23.38° and 22.66°, respectively, which are the SPR dip angles. As shown in the figure, the incident light begins to pass through the Au grating into the silicon, this lead to the decrease of the reflectance at angle without SPR occurring and also the low SPR coupling efficiency. As for the photodetector, a thinner Au layer produces higher quantum efficiency. However, when the Au layer is too thin, the FWHM of the SPR dip is large which will reduce the spectral resolution of the photodetector. With a thin Au layer, at non-SPR dip angle, the light can also produce a large photocurrent, which will decrease the signal to noise level of the photodetector at SPR dip angle and lead to a poor wavelength-selectivity. The Au layer with thickness larger than 60 nm is preferred for the current parameters of the simulated grating.

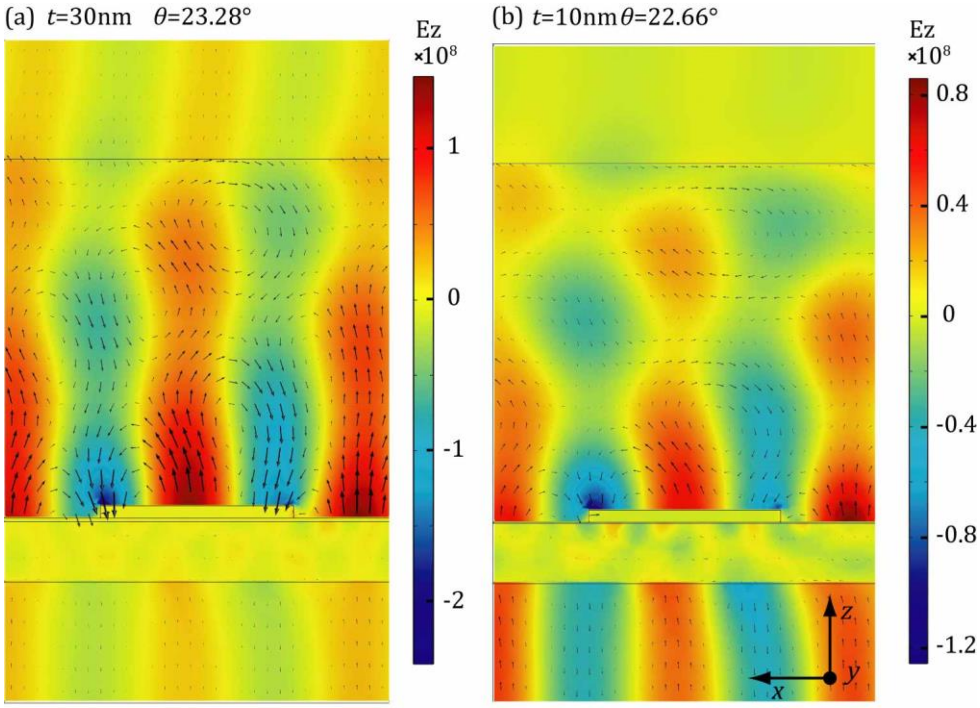

Figure 3.9 Simulated electric field of Au layer thickness of 10 nm and 30 nm at angle of 23.28° and 22.66° with SPR occurring.

Grating Pitch

The grating pitch is related to the angle of incidence where the SPR occurs. The Au gratings with pitches from 2 μm to 4 μm were also simulated with COMSOL. The other parameters of the grating are slit height of 100 nm, the Au layer thickness of 100 nm and fill factor of 0.5. The wavelength of the incident light is 1500 nm. The obtained reflectance curves are shown in **Figure 3.10**.

The SPR dip angle changes with the pitch. There are several SPR dips for each pitch corresponding to different diffraction orders. SPR dip angles of each pitch are obtained from the reflectance curve. The equations (**Equations (2.7)** and **(2.10)**) deducing the SPR coupling condition in Chapter 2 are used to relate the SPR dip angles with the diffraction orders. The calculated (Cal.) and simulated (Sim.) SPR dip angles along with the corresponding diffraction orders are shown in **Table 3.4**. The SPR dip angles from the calculation and the simulation are approximately consistent. Most of the differences are

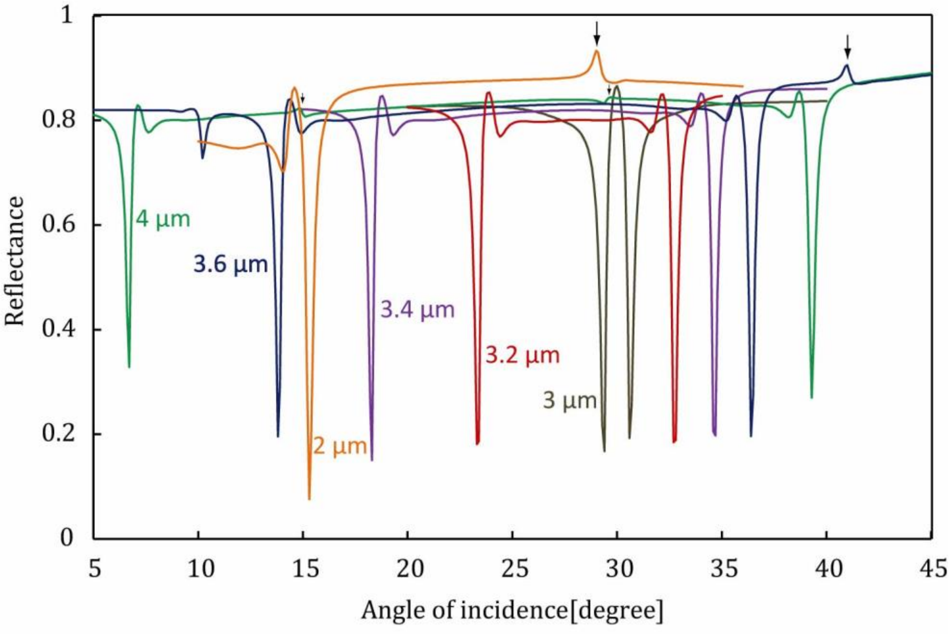

Figure 3.10 Simulated reflectance curves of pitch from 2 μm to 4 μm.

smaller than 0.3°, except that pitch of 2 μm in diffraction order of 1 has a difference of 0.5°. The differences are caused by the approximation of the SPPs dispersion relation in the calculation. In **Table 3.4**, the simulated SPR dip angle value in some cells of the table are blank. It is because these SPR dip angles were not covered in the angle range of the simulation. The symbol "-" indicates the SPR dip angle for the diffraction order does not exist.

When the grating pitch is a and the wavelength is λ, the diffraction order n in which the SPR dip angle exists can be estimated by the following equation [76]

$$\frac{1}{2n_d} < \frac{a}{\lambda} < \frac{1}{n_d},\ n = -1; \tag{3.2.1}$$

$$\frac{1}{n_d} < \frac{a}{\lambda} < \frac{3}{2n_d},\ n = 1, -2; \tag{3.2.2}$$

$$\frac{3}{2n_d} < \frac{a}{\lambda} < \frac{2}{n_d},\ n = 1, -2, -3; \tag{3.2.3}$$

Table 3.4 Calculated (Cal.) and simulated (Sim.) SPR dip angles of different diffraction orders n for grating pitch from 2 μm to 4 μm in range of 5°to 45°.

Pitch		$n = 1$	$n = 2$	$n = -2$	$n = -3$	$n = -4$
2μm	Cal .	14.81°	-	**29.62°**	-	-
	Sim .	15.3°	-	**29°**	-	-
3μm	Cal .	30.4°	0.33°	-	29.62°	83.87°
	Sim .	30.6°		-	29.4°	
3.2μm	Cal .	32.47°	3.9°	-	23.61°	60.38°
	Sim.	32.7°		-	23.35°	
3.4μm	Cal .	34.4°	7.1°	-	18.5°	49.37°
	Sim .	34.7°		-	18.3°	
3.6μm	Cal .	36.1°	9.9°	-	14.1°	**41.4°**
	Sim .	36.4°	10.2°	-	13.8	**41°**
4μm	Cal .	39.1°	**14.8°**	-	6.9°	**29.6°**
	Sim .	39.3°	**14.8°**	-	6.7°	**30°**

where n_d is the refractive index of the dielectric around grating. In this thesis, the dielectric is air with refractive index of 1. Replacing the values of pitches and wavelength of 1500 nm into the **Equation (3.2)**, the diffraction orders with SPR existence shown in **Table 3.4** are consistent with the equation.

In addition, as shown in **Figure 3.10** with arrows, at some angles, the SPR dips are replace by small peaks in some orders for pitch of 2μm, 3.6μm and 4μm, these angles are shown with bold font in **Table 3.4**. This is considered because the diffraction angles at these angles is very close to 90°, the peaks caused by the disappearance of the order and the dips caused by SPR are overlapped, the first effect dominates the reflection in these angles, therefore, peaks are shown in the reflectance curves. The angles with the disappeared diffraction calculated with **Equation (3.1)** are 30° for pitch of 2μm in diffraction order of -2; 41.8° for pitch of 3.6μm in diffraction order of -4; 14.47° and 30° for pitch of 4μm in diffraction order of -2 and -4 respectively. These angles are approximately consistent with the angles obtained from the peaks of the simulated reflectance curves shown with bold font in **Table 3.4**.

The pitch of the grating determines the distribution of the SPR dip angles. In order to achieve a broad detectable wavelength range, the value of the grating pitch should be chosen with widely separated adjacent SPR dip angles. In addition, the diffraction order in which the SPR dip is sharper should be selected to achieve high spectral resolution and high signal to noise ratio for SPR enhanced photocurrent.

Simulation on Grating Fill Factor

The fill factor of the grating is defined as dividing the width of the slab by the pitch. Au gratings with a pitch of 3.2μm varying the fill factor were also simulated. The wavelength of the incident light is 1500 nm. Both the height of the grating slit and the thickness of the Au layer are 100 nm. The simulated reflectance curves are shown in **Figure 3.11**.

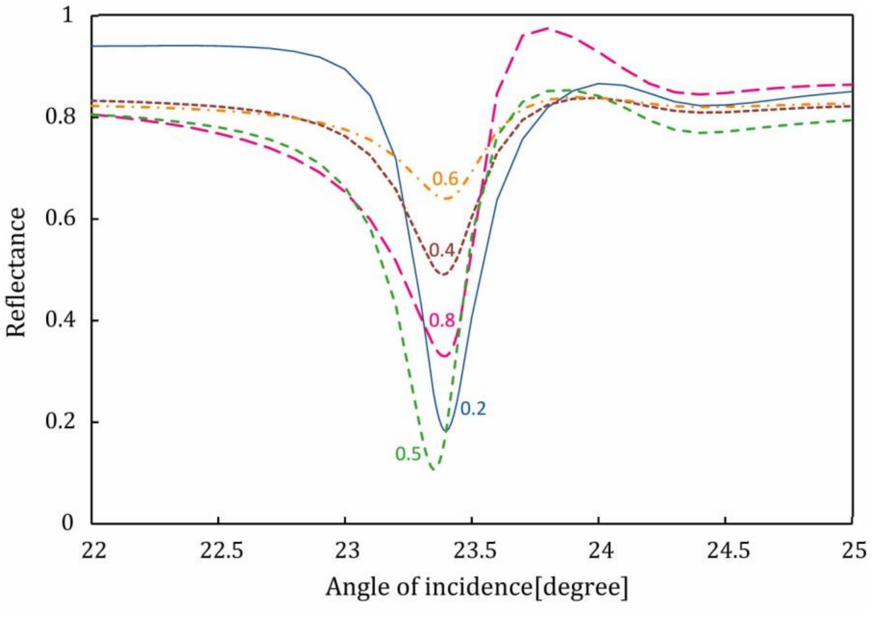

Fig. 3.11 Simulated reflectance curves varying fill factor from 0.2 to 0.8.

The SPR dip angles in the range correspond to the diffraction order of −3. The SPR dip angle of each fill factor is approximately the same as 23.4° except that the SPR dip angle of fill factor of 0.5 is 23.35°. The reflectance at SPR dip angle of fill factor of 0.2 is lower than that of 0.4. The reflectance at SPR dip angle of fill factor of 0.8 is lower than that of 0.6. According to the simulation, the fill factor of the grating affects the FWHM and the depth of SPR dip. Because the reflectance at SPR dip angle of fill factor of 0.5 is the lowest and the FWHM of it is the smallest among the simulated fill factors, fill factor of 0.5 is better than other values for the simulated grating profile.

3.2 Schottky Barrier Height

In order to detect the near infrared (NIR) light, the Schottky barrier height should be lower than the energy of the light. A Schottky photodiode was developed to calculate the barrier height of Au and n-type silicon.

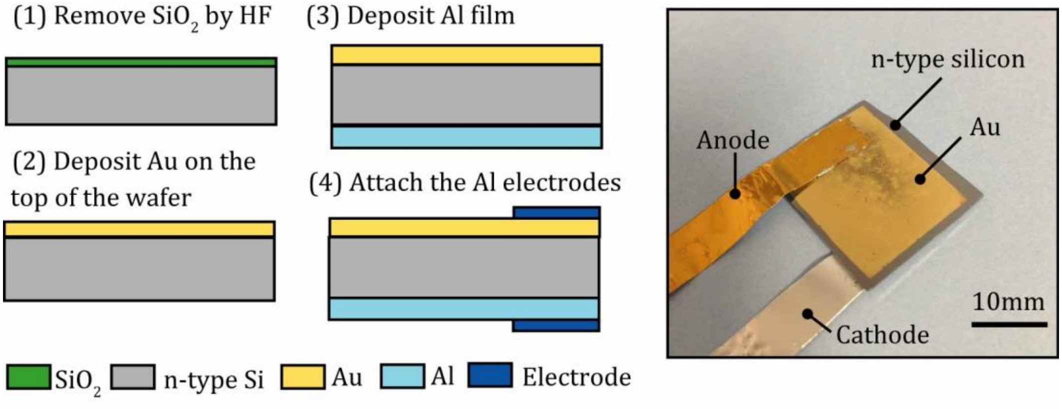

Fig. 3.12 Fabrication process and picture of the Schottky photodiode.

The fabrication process and the picture of the photodiode is shown in **Figure 3.12**. Firstly, the n-type silicon wafer (0.1~100 Ω · cm) was put into an HF solution for 1 minute to remove the thin silica film. Then, an Au film with thickness of 110 nm was deposited on the surface of the wafer. Then an Al film with thickness of 100 nm was deposited on the bottom of the wafer. The Au with the n-type silicon forms Schottky junction, while the Al and the n-type silicon forms ohmic contact. Finally, two Al electrodes were attached to the Au and Al film respectively. The electrode attached to the Au side was used as the anode of the photodiode, the one attached to the Al side was as cathode. A semiconductor parameter analyzer (HP, 4156B) measured the IV curve of the photodiode. The photodiode was put into a dark box at room temperature. The measured IV curve is shown in **Figure 3.13**. The voltage was varied from -1 V to 1 V. When the photodiode was applied reverse bias, the reverse saturation current was very small, while the current increased exponentially as applying forward voltage which proves that a Schottky junction is successfully formed by the Au and the n-type silicon wafer.

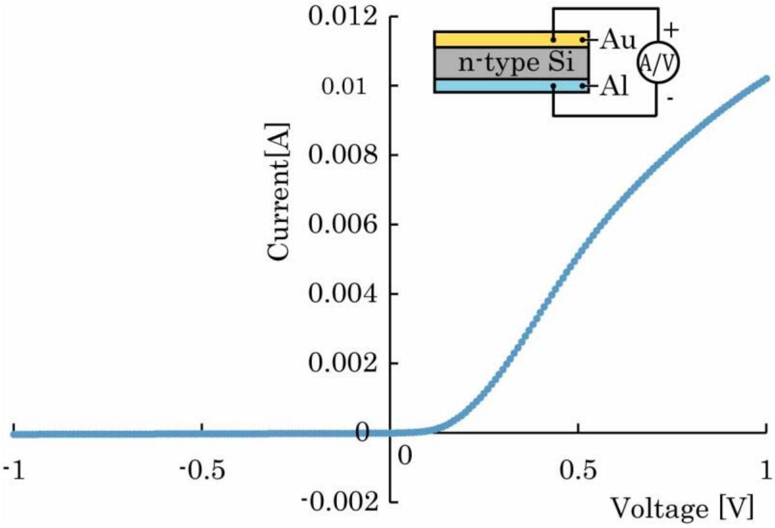

Fig. 3.13 IV curve of a Schottky photodiode.

The Schottky barrier height of the photodiode was calculated from the measured IV curve. The calculation method referred to the paper from S. K. Cheung and N. W. Cheung [77]. The forward bias part of the measured IV curve was used in the calculation. The relation of the applied voltage across the Schottky barrier (V_D) and the current (I) of a Schottky diode is described by the following equation [77]

$$I = I_s[\exp\left(\frac{qV_D}{nkT}\right) - 1] \tag{3.3}$$

$$I_s = A_{eff}A^{**}T^2\exp(-q\Phi_b/kT),$$

where the q is the elementary charge, k is the Boltzmann constant, n is the ideality factor, A_{eff} is the effective area of the diode, A^{**} is the Richardson constant and Φ_b is the Schottky barrier height. Part of the applied voltage is divided by the series resistance (R) of the Schottky, thus the left voltage applied to the Schottky barrier is calculated by subtracting the voltage on the resistance $V_D = V - IR$. Using the current density $J = \mathrm{I}/A_{eff}$ instead of the current to calculate the applied voltage, the **Equation (3.3)** becomes as follows:

$$V = RA_{eff}J + n\Phi_b + (n/\beta)\ln(J/A^{**}T^2) \tag{3.4}$$

$$\beta = q/kT.$$

We change the form of the above equation by differentiation.

$$\frac{d(V)}{d(lnJ)} = RA_{eff}J + \frac{n}{\beta} \tag{3.5}$$

In addition, the differentiation of the applied voltage and the current density can be changed to the following form.

$$\frac{d(V)}{d(lnJ)} = \frac{d(V)}{d(ln\frac{I}{A_{eff}})} = \frac{d(V)}{\frac{A_{eff}}{I}d(\frac{I}{A_{eff}})} = I\frac{d(V)}{d(I)} \tag{3.6}$$

Using the above equation, we can calculate $d(V)/d(lnJ)$ from the IV curve. According to **Equation (3.5)**, it should be linear to the current. Therefore we can obtain the n/β from the linear approximation curve of $d(V))/(d(lnJ)$. The calculated result of $d(V))/(d(lnJ)$ curve of the photodiode is shown in **Figure 3.14**. The calculated n approximately equals to 1.17, by taking the following values to $n/\beta = 0.0303$,

Elementary charge $q = 1.60218 \times 10^{-19}$ C

Boltzmann constant $k = 1.38066 \times 10^{-23}$ $\mathrm{m^2 kg\ s^{-2} K^{-1}}$

Room temperature $T = 300\mathrm{K}$

To obtain the barrier height, the following function is defined.

$$H(\mathrm{J}) \equiv \mathrm{V} - (\mathrm{n}/\beta)\ln(J/A^{**}T^2) \tag{3.7}$$

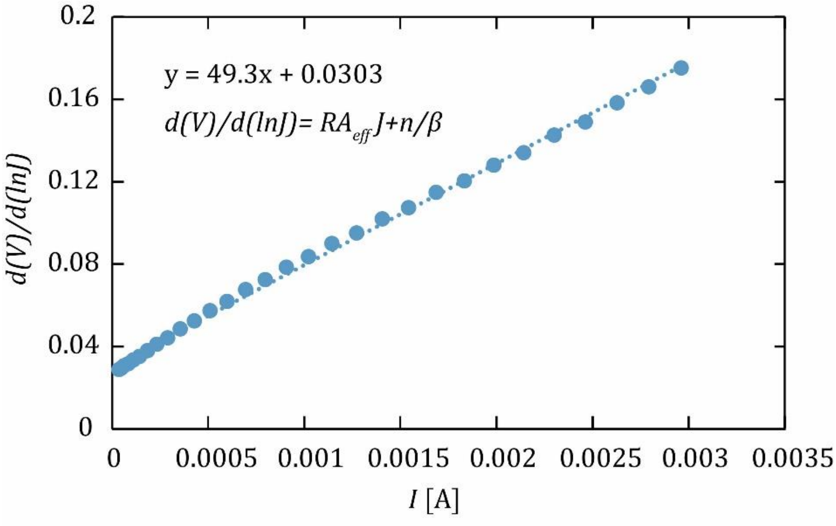

Fig. 3.14 Calculated curve of $d(V)/d(lnJ)$ verse I.

Substituting $J = I/A_{eff}$ into the above equation, we change equation to the following form, so that the function $H(\mathrm{J})$ can be extracted from the IV curve.

$$H(\mathrm{J}) \equiv \mathrm{V} - (\mathrm{n}/\beta)\ln(I/A_{eff}A^{**}T^{2}) \tag{3.8}$$

In addition, using the **Equation (3.4)**, we can obtain the following form of the function $H(\mathrm{J})$.

$$H(\mathrm{J}) = RA_{eff}J + n\Phi_{b} \tag{3.9}$$

The calculated function $H(\mathrm{J})$ of the photodiode is shown in **Figure (3.15)**. The Schottky barrier height can be calculated from the linear approximation curve of the function $H(\mathrm{J})$. The calculated Schottky barrier height is approximately 0.78 eV.

$$\Phi_{b} = \frac{0.9199}{n} \approx 0.78\ \text{eV}$$

The responsivity of the Schottky photodiode to the NIR light from 1470 nm to 1570 nm was also calculated by the measured photocurrent divided by the power of the incident light. A NIR laser source (Agilent, 8163B) was used to provide the incident light. The photocurrent of the photodiode was measured by a DC voltage current monitor (ADCMT, 6242). The power of the incident NIR light was measured by a power meter (ADVANTEST,

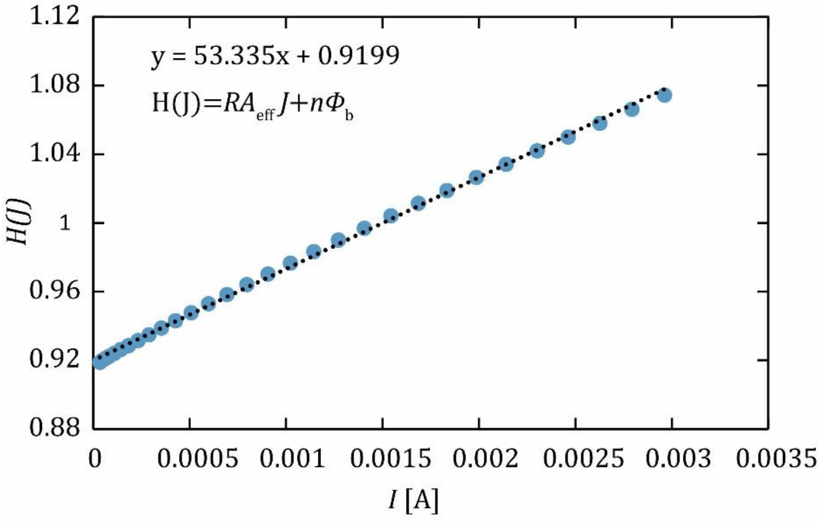

Fig. 3.15 Calculated curve of $H(\mathrm{J}) \equiv \mathrm{V} - (\mathrm{n}/\beta)\ln(I/A_{eff}A^{**}T^2)$verse I.

Q8221). The light was normally incident on the photodiode. The result is shown in **Figure 3.16**.

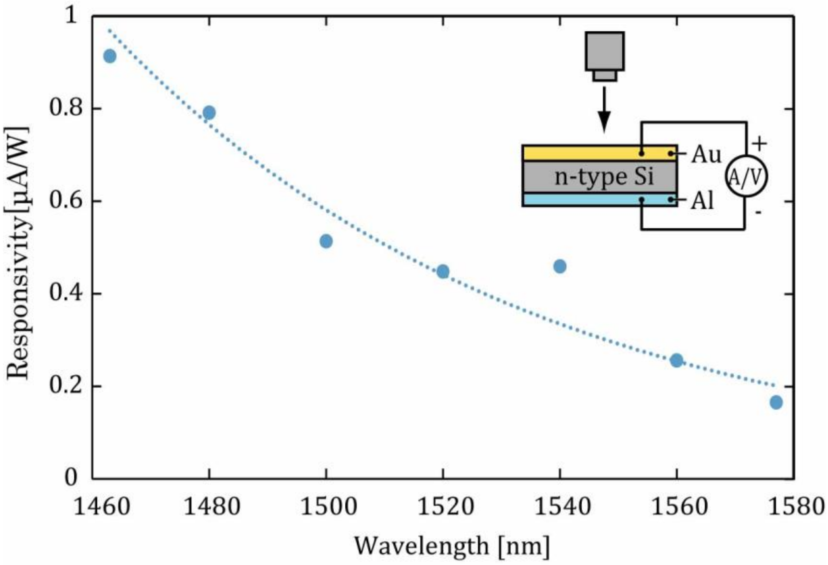

Fig. 3.16 Responsivity of the Schottky photodiode from 1463 nm to 1577 nm.

The measured wavelengths of the light were 1463 nm, 1480 nm, 1500 nm, 1520 nm, 1540 nm, 1560 nm and 1577 nm. The responsivity of the photodiode to light with wavelength of 1463 nm and 1577 nm was 0.91 μA/W and 0.16 μA/W respectively. Both the calculated Schottky barrier height and the responsivity testing results show that the Schottky junction formed by Au and n-type silicon is able to detect the NIR light.

3.3 Fabrication Process

The photodetector was fabricated on an n-type silicon wafer. The fabrication process is shown in **Figure 3.17.**

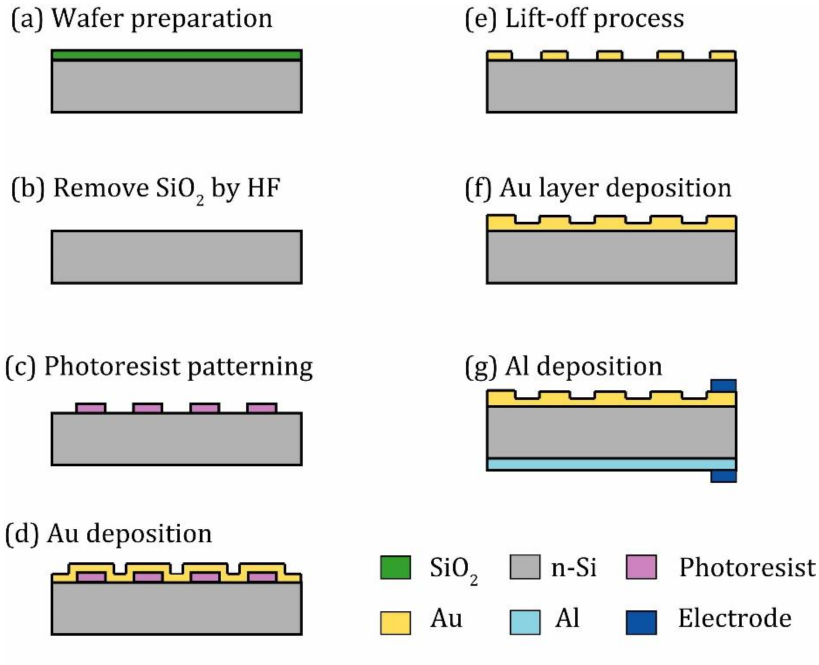

Fig. 3.17 Fabrication process of the photodetector.

(a) The silicon wafer was put into the cleaning water and cleaned by the ultrasonic wave. **(b)** The wafer was then put into a 1% hydrogen fluoride (HF) solution for 1 minute to remove the silica on the top of the wafer. **(c)** After removing the silica, the wafer was firstly put into an oven to dry the water left on the surface of the wafer, the temperature was set at 110°C and the drying time was set for 1 minute. Then, it was put on a spin-coating machine to deposit a uniform thin film of the photoresist. Thirdly, the wafer was put into the oven to dry for 1 minute at temperature of 110°C. Then, it was put on the SUSS Mask

Aligner, the photoresist was exposed to the ultraviolet light. The wafer then was put into the photoresist developer quickly, the beaker with the photoresist developer and wafer was gently shaken for 45 seconds. Because the photoresist used in this process is a positive photoresist, the pattern that was not sheltered by the photomask became soluble to the photoresist developer. As a result, a grating of photoresist was formed on the silicon surface. After checking the grating was successfully formed using the microscope, the wafer then was put into a buffered hydrofluoric acid (BHF) solution that is mixed by hydrogen fluoride and ammonium fluoride with a ratio of 1:6. The time was set for 30 second to remove the newly generated silica and clean the wafer, so that the deposited Au can make a good contact with the silicon surface in next step. **(d)** A film of Au was deposited on the surface of the wafer. The thickness of this Au film determined the height of the grating slit. **(e)** The wafer with deposited Au film was put into a photoresist stripping solution for 20 minutes. The Au on top of the photoresist started to separate from the wafer surface, however, because the grating pattern was in micrometer scale and the property of the photoresist changes due to the high temperature during the deposition process, the photoresist with Au on it could not totally removed in a short time. The wafer was then put into a new clean photoresist stripping solution and put into an ultrasonic wave cleaner to increase the speed of removing process. **(f)** After checking the Au grating was successfully fabricated in the microscope, the wafer was put into a BHF solution for cleaning. Then an Au film was deposited on the surface of the wafer. The thickness of this Au film determined the thickness of the Au layer of the grating. **(g)** Finally, a film of aluminum was deposited on the backside of the n-type silicon wafer to form an ohmic contact with the silicon. Then two aluminum tapes were attached to the Au grating surface and the aluminum film as two electrodes for experimental test.

In order to successfully fabricate the Schottky photodetector with an Au grating, there are several important points in the fabrication process. Firstly, the BHF solution is used to clean the wafer before depositing the Au film, which benefits the lift-off process to make the Au grating remain contacting to the silicon when the ultrasonic wave is used. Secondly, the development of photoresist should not be over-developed or under-developed, especially the latter. If there was even a very thin film of photoresist left on the silicon surface because of under- development, the Au deposited on top of it will be removed during the lift-off process, as a result, there will be no grating left after the lift-off process. If the photoresist is over-developed, the photoresist slit left is very slim. It is more difficult to remove the photoresist during the lift-off process. Thirdly, the top and the bottom surface of the wafer should be electrically insulated. In case of the Au on the top of the wafer contacted with the aluminum on the bottom surface of the wafer, the wafer edge was attached tapes during all the deposition processes. In addition, in the last step of attaching aluminum tape to the wafer, a conductive adhesive was used. It was dried in an oven for 5 minutes to become solid. The conductive adhesive becomes flexible then solid during the heating process, so it should not be spread near the edge of the wafer in case of contacting the top and back surface of the wafer.

3.4 Summary

In this chapter, the parameters of the Au grating were simulated using COMSOL Multiphysics. The SPR depth increases as the grating slit height becomes larger, however, the FWHM of the dip also becomes larger. A tradeoff is needed to make when the value of the grating slit height is designed. A relatively thick Au layer (larger than 60 nm) does not affect the SPR property of the grating, however, if the thickness is too small, the SPR dip become wider and shallow, which will reduce the signal to noise ratio and the spectral resolution of the photodetector. The pitch of the grating relates to the SPR dip angle and the diffraction orders for SPR occurring. The grating with pitch value to make the two adjacent SPR dip angle far away from each other should be chosen to achieve broad detectable wavelength range. The fill factor affects the depth and the FWHM of the SPR dip, while the dip angle is slightly shifted. Then, the height of the Schottky barrier formed by Au and n-type silicon was calculated from IV curve of a fabricated photodiode. The results showed that the barrier height is low enough for detecting NIR light from 1470 nm to 1570 nm. Finally, the fabrication process of the photodetector was introduced. Some important details in the fabrication process was presented.

Chapter 4 Experiment and Result

In this chapter, firstly, in order to confirm that SPPs are able to be excited and detected by the photodetector, the reflectance and photocurrent versus angle of incidence curves of a fabricated photodetector are firstly measured. Secondly, the experiments of spectrum measurement are introduced including the experimental steps, the information of the tested photodetector, the process of obtaining the responsivity matrix and the spectrum measurement of NIR light with single wavelength and multiple wavelengths by the photodetector and two commercial spectrometers for comparison.

4.1 Confirming SPR

4.1.1 Parameters of Tested Photodetector

A photodetector was fabricated to confirm that SPR occurs on the Au grating and photocurrent is generated by SPPs decay. The setting values of Au deposition in the ultra-high vacuum deposition machine for the slit height and the Au layer thickness are both 50 nm. The designed pitch and fill factor of the grating are 3.2 μm and 0.5. The picture of

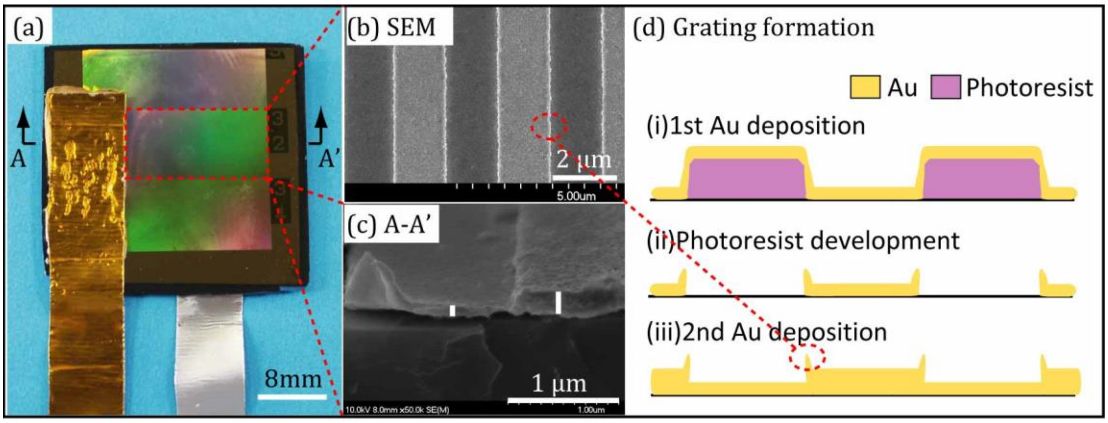

Fig. 4.1 (a) Picture of the tested photodetector **(b)** SEM image of Au grating **(c)** Side view of Au grating (d) Schematic illustration of grating formation.

the photodetector is shown in **Figure 4.1 (a)**. The pitch and fill factor were observed using Scanning Electron Microscope (SEM). As shown in **Figure 4.1 (b)**, both of the two parameters are approximately the same as the design values. The height of the grating slit and the thickness of Au layer were also measured by SEM. The photodetector was divided from the center and the side view of the grating is shown in **Figure 4.1 (c)**. The slit height is approximately 100 nm and the thickness of Au layer is approximately 98 nm. As shown in **Figure 4.1 (b)**, the edge of the slab of the grating slightly raised. As shown in **Figure 4.1 (d)**, it is because some of the Au on the photoresist was left during the process of photoresist development. However, the scale of the raised edge (nano-size) is much smaller than the scale of the grating (micro-size). It also much smaller than the wavelength of the NIR light. Therefore, this fabrication should have little effect on the responsivity of the photodetector. In addition, the characteristic parameter, the responsivity matrix, of each photodetector is calibrated before using it to detect the spectrum. Therefore, the responsivity matrix of each photodetector may be different, but this should not affect the spectrum measurement performance of the photodetector.

4.1.2 Experiment Setup

The experiment setup for measuring the reflection and photocurrent curves is shown in **Figure 4.2**. The light from the laser source passed through a polarizer then was incident

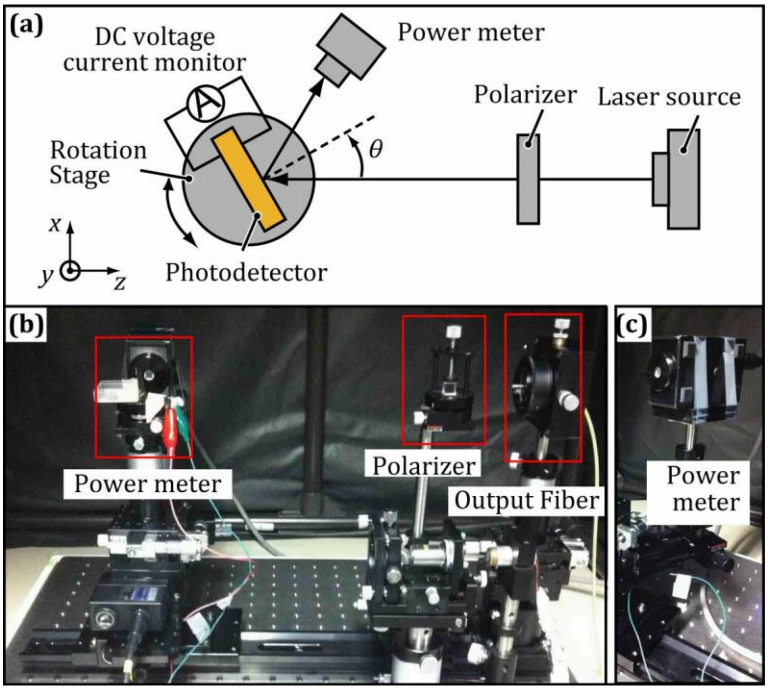

Fig. 4.2 **(a)** Schematic illustration of the experiment setup to measure photocurrent and reflection curves **(b)** Picture of the experiment setup **(c)** Picture of the power meter.

on the photodetector. The photodetector was put on a rotation stage, which was used to vary the angle of incidence of the light. The picture of the experiment setup is shown in **Figure 4.2 (b)**. Because the detecting head of the power meter is difficult to see from **(b)**,

出版予定のため非公開

出版予定のため非公開

Fig. 4.3 (a) Picture of photodetector (b) Arrangement of Au grating slit direction (c) Enlarged picture of Tilt/rotation stage.

出版予定のため非公開

出版予定のため非公開

[redacted]. In order to measure the reflected light simultaneously, the motor also rotated the detecting head of the power meter. Because the parameters of the stepping motor driven rotation stage determine the precision of the angle of incidence, they are shown in **Table 4.1**.

Table 4.1 Parameters of the stepping motor driven rotation stage.

Resolution of rotation (half)	0.0025°/pulse
Positioning Accuracy	0.1°
Positional Repeatability	0.02°

As shown in the above table, the resolution of the rotation stage is 0.0025°/pulse. The positioning accuracy is 0.1°. It is defined as the difference between the target angle values and the measured angle values at each position when the stage is successively rotated from a reference position. The positional repeatability of the rotation stage is 0.02°. In the following experiments in this thesis, the angle of incidence is varied by an interval of 0.1° using 40 pulse. It is in the working range of the rotation stage.

As shown in **Figure 4.3 (a)**, the electrode of the Au of the photodetector was connected to the positive detecting connector of the DC voltage current monitor. The electrode of the aluminum was connected to the ground. In this way, the detected Schottky circuit current by the light is negative. However, the photocurrent in this thesis is shown in positive value for convenience.

4.1.3 Alignment before Testing

出版予定のため非公開

出版予定のため非公開

出版予定のため非公開

Fig. 4.4 (a) Alignment of laser source **(b)** Adjustments of grating slit direction.

出版予定のため非公開

4.1.4 Measured SPR Curves

出版予定のため非公開

出版予定のため非公開

Fig. 4.5 Measured reflectance and photocurrent of a photodetector.

出版予定のため非公開

4.2 Spectrum Measurement

4.2.1 Experiment Steps

出版予定のため非公開

出版予定のため非公開

出版予定のため非公開

Fig. 4.6 Steps of using a photodetector to measure spectrums.

出版予定のため非公開

Fig. 4.7 (a) Picture of the photodetector used in spectrum measurement **(b)** SEM Image of the fracture surface of the photodetector **(c)** Measured parameters.

4.2.2 Parameters of Tested Photodetector

The photodetector used in the following experiments is shown in **Figure 4.7 (a).** It has

出版予定のため非公開

4.2.3 Responsivity Matrix

Photocurrent Curves and SPR Dip Angles

The wavelength range from 1470 nm to 1570 nm was divided into 21 wavelength components with interval of 5nm (1470, 1475, 1480… 1570 nm). In order to construct the responsivity matrix, 21 groups of photocurrent curves were firstly measured. The picture of experiment setup is shown in **Figure 4.8**. Most of the setup are the same as those used

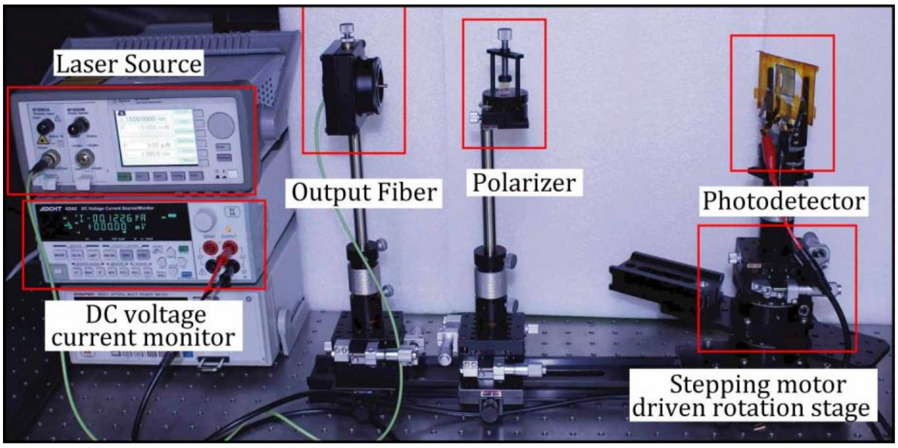

Fig. 4.8 Picture of experiment setup to measure photocurrent curves.

in section 4.1 except measuring the reflected light by the power meter.

The measured 21 groups of photocurrent curves are shown in **Figure 4.9**. The angle of incidence was varied from 18° to 30° with a resolution of 0.1°. The photocurrent of each

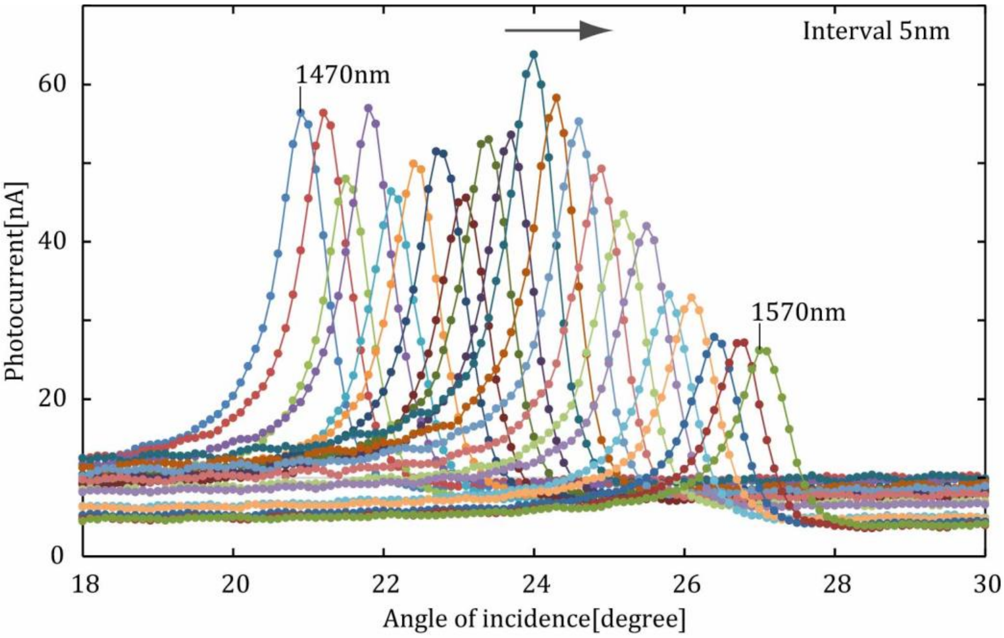

Fig. 4.9 Measured photocurrent curves of wavelength from 1470 nm to 1570 nm with the interval of 5 nm.

wavelength was measured at each angle. The measured photocurrent curves of wavelength of 1470 nm and 1570 nm are pointed out in the figure. There was a peak in each curve due to the enhancement of SPR. The angle of the peak is the SPR dip angle of the wavelength. With the wavelength increasing, the SPR dip angle became larger. Because the photon energy tends to decrease with an increase in the wavelength, the obtained maximum photocurrent had a tendency to decrease along with the increase of the wavelength. However, some photocurrents of longer wavelengths are larger than shorter wavelength (for example photocurrent of 1485 nm is larger than 1480 nm). It is mainly because the power of each wavelength was slightly different due to the spectral efficiency of the output optical fiber of the light source. Besides, the maximal photocurrents of some longer wavelengths are larger than shorter wavelength. It is mainly because the SPR coupling efficiency of these wavelengths are higher and more energy of the light is changed into photocurrent. However, these differences of photocurrents have slightly effect on the calculation of responsivity matrix, because the power of each wavelength was also measured to obtain the responsivity, which will be shown in the next section.

The SPR dip angle of each wavelength observed from the photocurrent curve is shown

出版予定のため非公開

Fig. 4.10 SPR dip angles from the COMSOL simulation, theoretical calculation and experimental results.

in **Figure 4.10**. These SPR dip angles are corresponding to the diffraction order of -3. The calculated values using equations in Chapter 2 and the simulated values using COMSOL

出版予定のため非公開

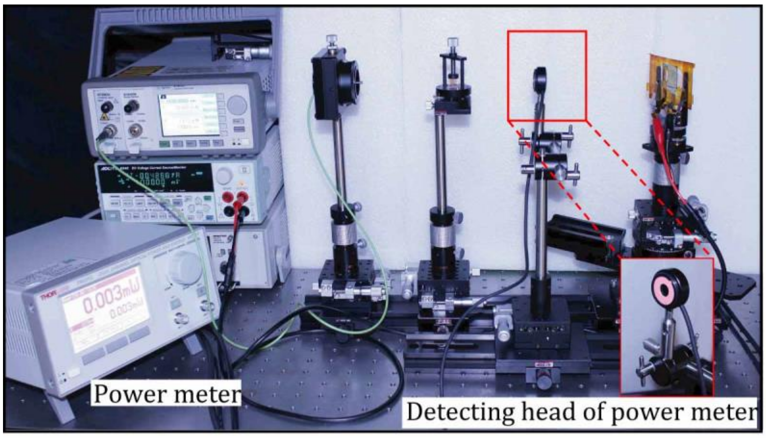

Fig. 4.11 Experiment setup to measure the power of the NIR light.

Power of Incident Light

In order to calculate the responsivity, the power of the NIR light of each wavelength was also measured. The output power of the tunable laser source was set as 10mW. It is the same as the value used to obtain the photocurrent curves. The experiment setup of the measurement is shown in **Figure 4.11**. A NIR light power meter (Thorlabs, PM320E-SC122C) was used to measure the power. The detectable wavelength range of it is 700 nm to 1800 nm. The detecting head of it was placed between the polarizer and the testing

Table 4.2 Measured power of incident light with wavelength from 1470 nm to 1570 nm.

Wavelength[nm]	**1470**	**1475**	**1480**	**1485**	**1490**	**1495**	**1500**
Power[mW]	1.364	1.194	1.315	1.752	1.952	2.382	2.381
Wavelength[nm]	**1505**	**1510**	**1515**	**1520**	**1525**	**1530**	**1535**
Power[mW]	2.484	2.483	2.37	2.8	2.48	2.54	2.34
Wavelength[nm]	**1540**	**1545**	**1550**	**1555**	**1560**	**1565**	**1570**
Power[mW]	2.255	2.4	2.58	2.74	2.26	3.03	2.35

photodetector. The measured results are shown in **Table 4.2**. The measured power of each wavelength was different and smaller than the setting value. It is because the light lost power during transporting in the output fiber. The attenuation depends on the wavelength. In addition, because the light passed through the polarizer, only the transverse magnetic polarized light was left. As a result, the incident power became smaller than half of the setting value.

Calibration of Responsivity Matrix

The wavelength range from 1470 nm to 1570 nm was divided into 21 components. Therefore, the responsivity matrix is a 21×21 matrix. The entries of the responsivity matrix were calculated by the photocurrents at SPR dip angles dividing by the power of the NIR light (**Equation 2.21**).

出版予定のため非公開

Table 4.3 Measured 21×21 responsivity matrix.

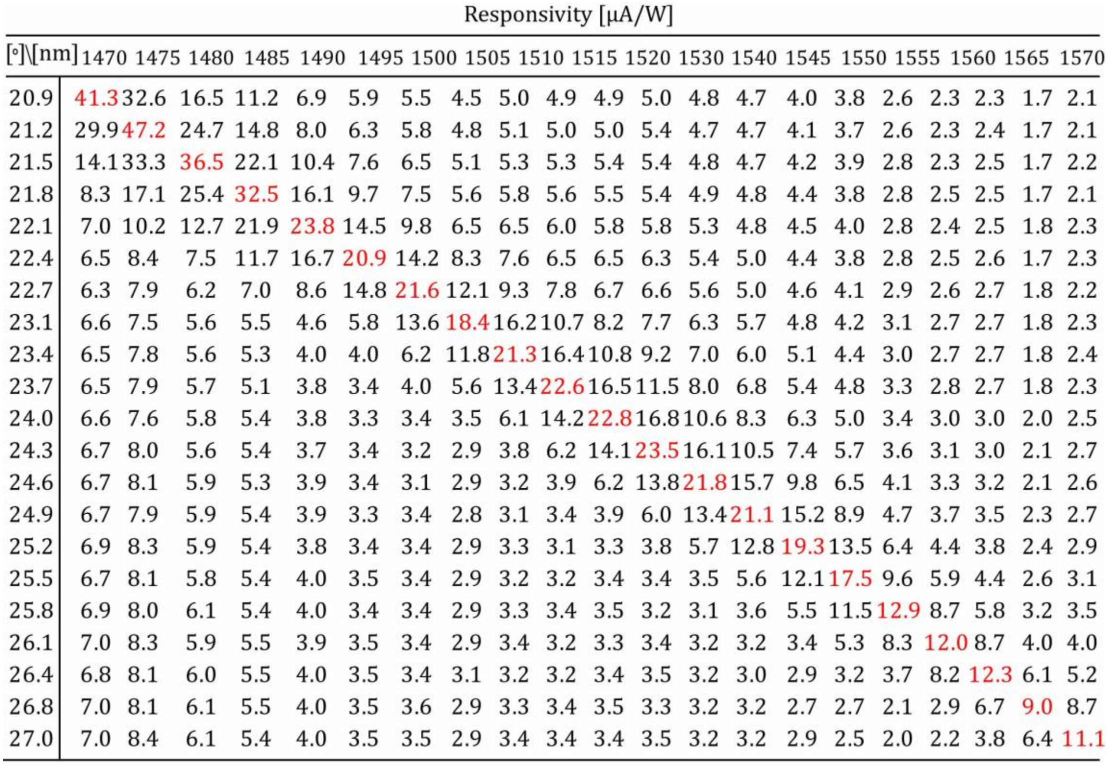

Responsivity [μA/W]

[°]\[nm]	1470	1475	1480	1485	1490	1495	1500	1505	1510	1515	1520		1530		1540	1545	1550	1555	1560	1565	1570
20.9	41.3	32.6	16.5	11.2	6.9	5.9	5.5	4.5	5.0	4.9	4.9	5.0	4.8	4.7	4.0	3.8	2.6	2.3	2.3	1.7	2.1
21.2	29.9	47.2	24.7	14.8	8.0	6.3	5.8	4.8	5.1	5.0	5.0	5.4	4.7	4.7	4.1	3.7	2.6	2.3	2.4	1.7	2.1
21.5	14.1	33.3	36.5	22.1	10.4	7.6	6.5	5.1	5.3	5.3	5.4	5.4	4.8	4.7	4.2	3.9	2.8	2.3	2.5	1.7	2.2
21.8	8.3	17.1	25.4	32.5	16.1	9.7	7.5	5.6	5.8	5.6	5.5	5.4	4.9	4.8	4.4	3.8	2.8	2.5	2.5	1.7	2.1
22.1	7.0	10.2	12.7	21.9	23.8	14.5	9.8	6.5	6.5	6.0	5.8	5.8	5.3	4.8	4.5	4.0	2.8	2.4	2.5	1.8	2.3
22.4	6.5	8.4	7.5	11.7	16.7	20.9	14.2	8.3	7.6	6.5	6.5	6.3	5.4	5.0	4.4	3.8	2.8	2.5	2.6	1.7	2.3
22.7	6.3	7.9	6.2	7.0	8.6	14.8	21.6	12.1	9.3	7.8	6.7	6.6	5.6	5.0	4.6	4.1	2.9	2.6	2.7	1.8	2.2
23.1	6.6	7.5	5.6	5.5	4.6	5.8	13.6	18.4	16.2	10.7	8.2	7.7	6.3	5.7	4.8	4.2	3.1	2.7	2.7	1.8	2.3
23.4	6.5	7.8	5.6	5.3	4.0	4.0	6.2	11.8	21.3	16.4	10.8	9.2	7.0	6.0	5.1	4.4	3.0	2.7	2.7	1.8	2.4
23.7	6.5	7.9	5.7	5.1	3.8	3.4	4.0	5.6	13.4	22.6	16.5	11.5	8.0	6.8	5.4	4.8	3.3	2.8	2.7	1.8	2.3
24.0	6.6	7.6	5.8	5.4	3.8	3.3	3.4	3.5	6.1	14.2	22.8	16.8	10.6	8.3	6.3	5.0	3.4	3.0	3.0	2.0	2.5
24.3	6.7	8.0	5.6	5.4	3.7	3.4	3.2	2.9	3.8	6.2	14.1	23.5	16.1	10.5	7.4	5.7	3.6	3.1	3.0	2.1	2.7
24.6	6.7	8.1	5.9	5.3	3.9	3.4	3.1	2.9	3.2	3.9	6.2	13.8	21.8	15.7	9.8	6.5	4.1	3.3	3.2	2.1	2.6
24.9	6.7	7.9	5.9	5.4	3.9	3.3	3.4	2.8	3.1	3.4	3.9	6.0	13.4	21.1	15.2	8.9	4.7	3.7	3.5	2.3	2.7
25.2	6.9	8.3	5.9	5.4	3.8	3.4	3.4	2.9	3.3	3.1	3.3	3.8	5.7	12.8	19.3	13.5	6.4	4.4	3.8	2.4	2.9
25.5	6.7	8.1	5.8	5.4	4.0	3.5	3.4	2.9	3.2	3.2	3.4	3.4	3.5	5.6	12.1	17.5	9.6	5.9	4.4	2.6	3.1
25.8	6.9	8.0	6.1	5.4	4.0	3.4	3.4	2.9	3.3	3.4	3.5	3.2	3.1	3.6	5.5	11.5	12.9	8.7	5.8	3.2	3.5
26.1	7.0	8.3	5.9	5.5	3.9	3.5	3.4	2.9	3.4	3.2	3.3	3.4	3.2	3.2	3.4	5.3	8.3	12.0	8.7	4.0	4.0
26.4	6.8	8.1	6.0	5.5	4.0	3.5	3.4	3.1	3.2	3.2	3.4	3.5	3.2	3.0	2.9	3.2	3.7	8.2	12.3	6.1	5.2
26.8	7.0	8.1	6.1	5.5	4.0	3.5	3.6	2.9	3.3	3.4	3.5	3.3	3.2	3.2	2.7	2.7	2.1	2.9	6.7	9.0	8.7
27.0	7.0	8.4	6.1	5.4	4.0	3.5	3.5	2.9	3.4	3.4	3.4	3.5	3.2	3.2	2.9	2.5	2.0	2.2	3.8	6.4	11.1

Inverse Matrix of the Calibrated Responsivity Matrix

出版予定のため非公開

As shown in the figure, the waveform of each row vector has a peak with a shape of "W" and other entries are near zero. The multiplication result of a row vector of matrix $\boldsymbol{R}^{-1}$ with the column vector $\boldsymbol{I}$ is the incident power of certain wavelength. For example, the multiplication of the first row with the column vector $\boldsymbol{I}$ becomes the power of the wavelength of 1470 nm. As show in **Figure 4.12**, the peak value of the first row (Row 1) is the first entry. The first entry will multiply with the photocurrent at the SPR dip angle of 1470 nm (20.9°). Because the first entry is larger than other entries in the row, it will give a larger multiplication factor to the photocurrent at the SPR dip angle of 1470 nm (20.9°)

than to other photocurrent values. This presents the wavelength-selectivity of the photodetector at SPR dip angle of 1470 nm (20.9°). At SPR dip angle of 1470 nm, the total photocurrent was mainly from its corresponding SPR wavelength of 1470 nm. The photocurrent from other wavelengths was very small without the SPR enhancement. As shown in **Figure 4.12**, the peak of the row vector shifts to the next adjacent entry to select the photocurrent of the next wavelength. The peak shifts from the first entry corresponding to 1470 nm to the last entry corresponding to 1570 nm.

We can use the "W" shape waveform of each row vector of the matrix $\boldsymbol{R}^{-1}$ to judge whether a responsivity matrix is able to calculate the spectrum or not. Because even the responsivity matrix is invertible in mathematics, it may not be able to calculate a spectrum. According to the above analysis, the measured responsivity matrix presents the wavelength-selectivity of the photodetector. We can use it to calculate the spectrum in the following experiments.

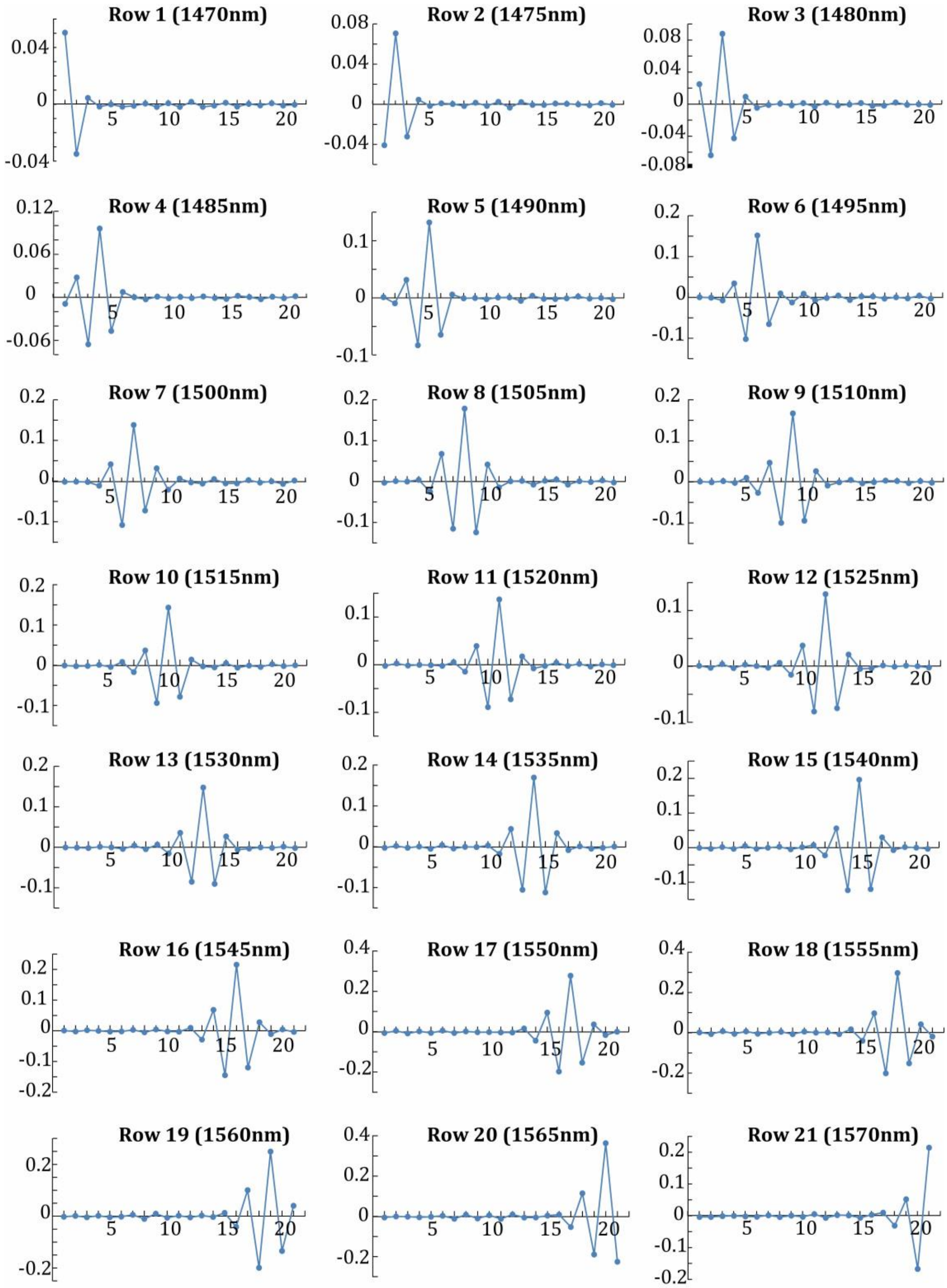

Fig. 4.12 Row vectors of inverse matrix ($\boldsymbol{R}^{-1}$) of the measured responsivity matrix.

4.2.4 Spectrum

Experiment Setup

In the experiments of measuring spectrum, a whitelase supercontinuum source (FIANIUM, SC450-2) along with an Integrated Acousto-Optic Tunable Filter (AOTF) (FIANIUM, NIR2) were used to provide the testing light. The pictures of the laser source are shown in **Figure 4.13**. The wavelength range of the whitelase source is from 450 nm to 2400 nm. The fundamental pulse width is 6 ps and the fundamental repetition rate is 20 MHz. The power stability is lower than ±1%. The broad band light from the whitelase source is input to the AOTF, which determines the output wavelength. The wavelength is set through a computer into the controller of the AOTF. The parameters of the AOTF are shown in **Table 4.4**. The output wavelength range of it is from 1100 nm to 2000 nm. It has eight simultaneous tunable wavelength channels. The channel bandwidth is approximately from 4 nm to 16 nm. The testing NIR light with single wavelength used

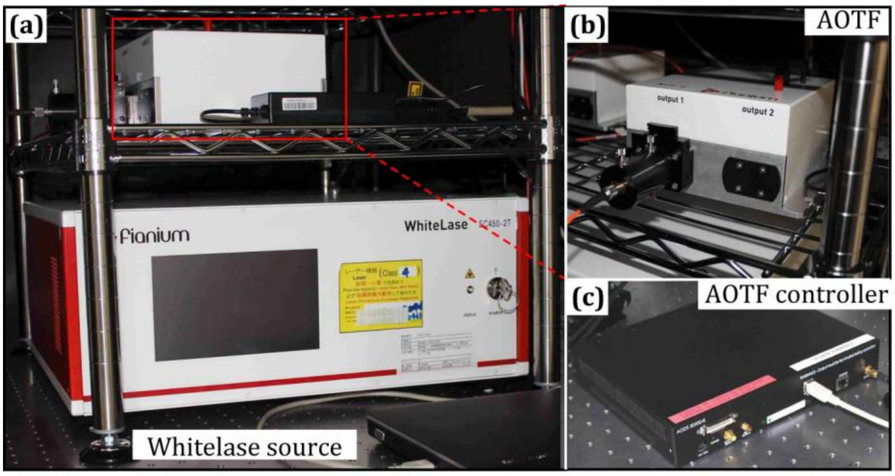

Fig. 4.13 (a) Whitelase source **(b)** AOTF **(c)** AOTF controller.

Table 4.4 Parameters of AOTF.

Wavelength range	1100 nm to 2000 nm
Number of wavelength channels	8
Channel bandwidth	4-16 nm
Polarization	Linear un-polarized

one channel of the AOTF, while several channels worked simultaneously to output light with mixed multiple wavelengths.

The picture of the experiment setup for the spectrum measurement using the photodetector is shown in **Figure 4.14**. The whitelase source was used instead of the previous tunable laser source. The other parts of the setup remained the same. The testing NIR light passed the polarizer. The rotation stage changed the angle of incidence to be the SPR dip angles, which were obtained in the calculation of the responsivity matrix. The DC voltage current monitor measured the photocurrent.

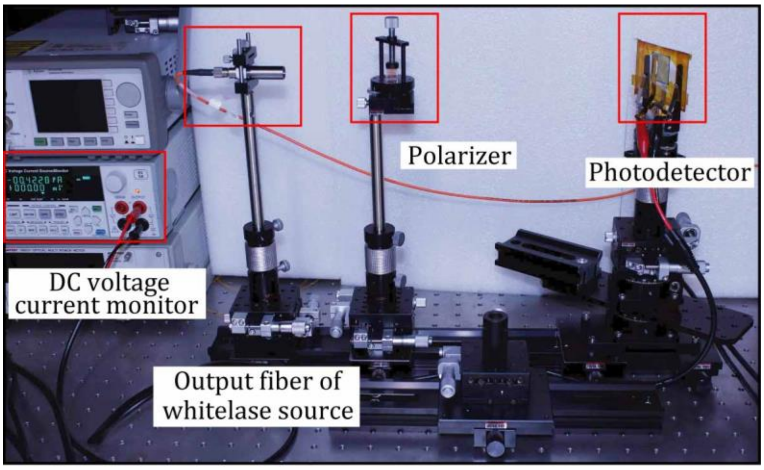

Fig. 4.14 Experiment setup for spectrum measurement by photodetector.

During the process of replacing the laser source, it is necessary to align the direction of the output light to make sure that the SPR dip angles were the same as the ones used to construct the responsivity matrix. The angle of incidence at the initial position of the rotation table should still be zero degree. The NIR light power meter (Thorlabs, PM320E-SC122C) was used to complete the replacement. Before removing the output fiber of the tunable laser source, the power meter detecting head was placed behind the polarizer. It was adjusted to where the light spot from the tunable laser source is right on the center of its sensing area. Then the output fiber of the whitelase source was mounted. We adjusted the position of it to make that the light spot also located in the center of the detecting area of the power meter as the previous laser source.

出版予定のため非公開

The second spectrometer delivers the spectral resolution of 5nm FWHM. The experiment setup using the two spectrometers to measure the NIR light is shown in **Figure 4.15**. An input fiber placed behind the polarizer was used to transport the testing NIR light to the two spectrometers.

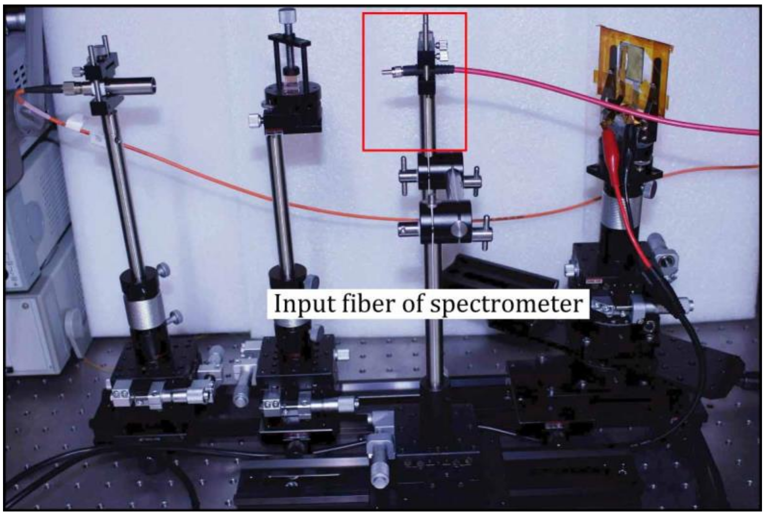

Fig. 4.15 Experiment setup for spectrum measurement by the two commercial spectrometers.

Spectrum of Light with Single Wavelength

The NIR light from the whitelase source with single wavelength was measured by the photodetector. The measured wavelengths were from 1470 nm to 1570 nm with the interval of 10 nm. In order to obtain the spectrums, the photocurrent at SPR dip angles of each wavelength was firstly detected. These photocurrent values formed a column vector ($\boldsymbol{I}$). The 11 groups of column vectors of the tested light are shown in **Table 4.5**. The maximal photocurrent of each column is in red color, the angle of it is consistent with the SPR dip angle of the input wavelength. Therefore, the measured photocurrent represented the wavelength of the tested light.

Firstly, the power distribution of each wavelength $\boldsymbol{P}$ was calculated by the

Table 4.5 Measured 11 photocurrents vectors of wavelength from 1470 nm to 1570 nm at SPR dip angles.

出版予定のため非公開

photocurrent column vector and the inverse matrix of the responsivity matrix ($\boldsymbol{P} = \boldsymbol{R}^{-1}\boldsymbol{I}$). The spectrums then were obtained by normalizing $\boldsymbol{P}$. The normalization was performed in Microsoft Excel and used the following equation

$$P_{nor} = \frac{P - P_{min}}{P_{max} - P_{min}} \tag{4.1}$$

where P_{min} is the minimal value of each column and P_{max} is the maximal value.

The two commercial spectrometers also measured the spectrums. The measured spectrums also used the above equation for normalization. The results from the photodetector and the two commercial spectrometers are shown in **Figure 4.16**. There were 11 input wavelengths from 1470 nm to 1570 nm in the experiment. Each input wavelength is written on top of the small figure, which shows the measured spectrums of the wavelength. The red points were the measured spectrum from the photodetector (PD).

出版予定のため非公開

出版予定のため非公開

The measured maximal wavelength and FWHM of each spectrum are shown in **Table 4.6.** The spectrums measured by the three methods were approximately the same. Firstly, for all the 11 wavelengths, the maximal wavelength (peak wavelength) of the spectrums by the three methods were approximately consistent.

出版予定のため非公開

Finally, the measured spectrums of the short wavelength and longer wavelength have a uniform precision. Therefore, the performance of the photodetector is not affected by the decrease of responsivity of the longer wavelength. The above experimental results show that the photodetector is able to measure the spectrum of light with single wavelength with a high precision in peak wavelength and FWHM. Its performance is comparable to those of the two commercial spectrometers.

Table 4.6 Maximal wavelength and FWHM measured by the two commercial spectrometers (S1 and S2) and the photodetector (PD).

出版予定のため非公開

出版予定のため非公開

Fig. 4.16 Measured spectrums by photodetector and two commercial spectrometers of the input light with wavelength from 1470 nm to 1570 nm.

Spectrum of Light with Multiple wavelengths

Spectrums of 6 groups of NIR light with mixed multiple wavelengths components were measured by the photodetector and the two commercial spectrometers. The multiple wavelengths were simultaneously incident on the surface of the photodetector. The wavelength components contained in each group of the light are shown in **Table 4.7**.

Table 4.7 Wavelength components of the measured 6 groups of NIR light.

出版予定のため非公開

In the experiment, firstly, the groups of (I) and (II) with three wavelength components were tested. The interval of the three wavelengths is 30 nm. The measured photocurrent curves are shown in **Figure 4.17 (a)**. The spectrums from the photodetector and from the

出版予定のため非公開

出版予定のため非公開

Fig. 4.17 (a) Photocurrent of the photodetector (PD) and spectrums of light with multiple wavelengths by the PD,

出版予定のため非公開

出版予定のため非公開

Secondly, the spectrums of groups of (III) and (IV) were measured. The results were shown in **Figure 4.17 (a)** and **(b)** respectively. Each group of light has four components with a smaller interval of 20 nm. The two spectrums measured by the photodetector were also approximately consistent with those measured by the two spectrometers. The

出版予定のため非公開

出版予定のため非公開

Fig. 4.17 (b) Photocurrent of the photodetector (PD) and spectrums of light with multiple wavelengths by the PD

出版予定のため非公開

出版予定のため非公開

出版予定のため非公開

Discussion on Spectral Resolution of Photodetector

出版予定のため非公開

出版予定のため非公開

Fig. 4.18 Illustration of (a) discriminable two adjacent SPR curves (b) wavelength resolution of responsivity matrix.

出版予定のため非公開

出版予定のため非公開

出版予定のため非公開

出版予定のため非公開

出版予定のため非公開

出版予定のため非公開

出版予定のため非公開

Fig. 4.19 Obtained photocurrent curves of wavelength of 1500 nm in two measurements.

出版予定のため非公開

4.3 Summary

In this chapter, firstly, the reflectance and photocurrent of a fabricated photodetector were measured. The results prove that the SPR was excited on the surface of the photodetector and the photocurrent presented the property of the SPR. Secondly,

出版予定のため非公開

groups of NIR light with multiple wavelengths were also measured by the three methods. The experiment results prove that the photodetector can achieve a comparable spectral

出版予定のため非公開

Conclusion

5.1 Conclusion

In this thesis, a photodetector enhanced by SPR was firstly utilized to achieve the spectrum measurement in NIR range of 1470 nm to1570 nm. The method in this thesis provides an option for realizing small-scale spectrometers with high spectral resolution, which overcomes the issue of spectral resolution limitation by optical path in diffraction grating based spectrometers. The comparison of several common spectrum measurement methods is shown in **Table 5.1.** In the conventional grating based spectrometers, the diffraction of gratings is used to separate different wavelength. The longer the optical path is, the wider the wavelengths are separated. When the scale of the spectrometers become smaller, we have to make a tradeoff between the optical path and the resolution. As a result, grating based micro-spectrometers have low resolution. In this thesis, the SPR instead of the diffraction of a grating directly couples the light. The grating is combined with a Schottky photodetector. There is no need of an optical path. In addition, the SPR light coupling has high SNR property and thus a high spectral resolution can be achieved.

The photodetector was formed by an Au grating on top of an n-type silicon wafer and aluminum film on bottom of the wafer. The Au grating wavelength-selectively couples the

Table 5.1 Comparison of different NIR spectrum measurement methods

	Advantage	Disadvantage
Diffraction grating and PD array	● Low cost and wide applications in compact NIRS	● Need of optical path ● Trade off on scale and resolution
SPR on grating and PD (Method in thesis)	● No optical path ● Photocurrent enhancement ● High resolution	● Need of varying angle of incidence
FP cavity and PD	● High resolution ● Small scale	● Need of optical path ● Needs of high reflectivity and flatness in two mirrors of cavity
FTIR	● High resolution	● Need of a complex system

light into SPPs and the Schottky junction formed by Au and n-type silicon collects the hot electrons generated by SPPs decay. Because the SPR coupling condition of a grating depends on the angle of incidence and the wavelength of the incident light, the SPR coupling has wavelength-selective characteristic at certain angle. The photodetector thus is wavelength-selective at SPR dip angle. A responsivity matrix was proposed to calculate the spectrum from the photocurrent versus angle of incidence curve. The responsivity matrix is a characteristic parameter of a photodetector hence can be pre-calibrated and repeatedly used for testing spectrums.

The spectrum of NIR light with narrowband single wavelength and mixed multiple wavelengths were measured by the photodetector.

出版予定のため非公開

出版予定のため非公開

The spectral resolution of the photodetector can be further improved by optimizing the design of the grating to have a sharper SPR dip. According to the simulation in Chapter 3, the parameters of the Au grating, the grating slit height, the Au layer thickness, the pitch and the fill factor affect the FWHM of the SPR dip. Optimizing these parameters provide a sharper SPR dip. In addition, the material, Au, of the grating can be change to metal with a small loss such as aluminum. The wavelength resolution of the obtained spectrum and the resolution of angle is also can be improved. Reverse bias voltage was not applied on the tested photodetector. The photodetector can work under strong light irradiation. The spectrum measurement process of the photodetector controlled by a computer can achieve high-speed measurement.

There are several future application fields for this work. Firstly, the method in this thesis can be used in various wavelength range spectroscopy. The mechanism of the spectrum measurement is based on the wavelength-selective light coupling by SPR. Other SPR coupling methods such as subwavelength gratings, nano-antennas can be used to replace the grating for coupling light and enhancing the responsivity of the photodetector in a wide wavelength range. The gratings can also be integrated with other types of photodetector and with the advantage of other type of photodetectors like high quantum efficiency and so on.

Secondly, the method in this thesis can be used for NIR spectrum imager. The fabrication process of the photodetector is compatible with the standard semiconductor fabrication process. If the photodetector is fabricated in array, a NIR imager could be achieved. Because single photodetector can obtain a spectrum. The imager could provide the spectral information as well as the spatial information of the sample, which is called hyperspectral imaging and it is widely used in NIR spectroscopy [79].

Finally, the photodetector in this thesis can be used for realizing compact spectrometer with high resolution. Without the limitation of optical path length, a miniature spectrometer can be developed through combining the photodetector with a micro-collimator. In addition, it could be integrated with micro-actuators to achieve a micro-spectrometer with high spectral resolution.

Appendix

Appendix A: Fabrication Flow of Photodetector

Cross Section	Process		Condition
	Wafer Preparation	n-type silicon wafer (0.1~100 Ω-cm, 625μm)	25 mm × 25 mm Wafer slice
	Wafer Cleaning	Remove SiO_2 by HF	1% HF dipping 1 min 1st water rinse 2nd water rinse
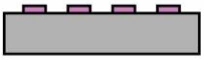	Photoresist Patterning	Spin coat photoresist	Spin coating OFPR23cp Prebake 110℃ 1 min 500 rpm × 8 sec 4000 rpm × 30 sec Bake 110℃ 1 min
		Develop photoresist	Exposure 1.8 sec Developer NMD3 60 sec 1st water rinse 2nd water rinse
		Check the grating pattern by microscope	Asing O_2 plasma 5 sec Checking no photoresist is left over the silicon surface of grating groove
		Cleaning	BHF Cleaning 30 sec 1st water rinse 2nd water rinse
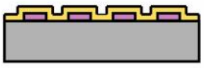	Au Deposition	Deposit Au on the surface of the wafer	4×10^{-2} Pa Thickness: 50 nm Deposition rate: 0.1 nm/s

Fig. A.1 Fabrication process of the Schottky photodetector with an Au grating (1/2)

Cross Section	Process		Condition
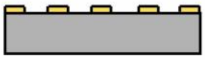	Liftoff Process	Dip the wafer in stripper solution Remove photoresist by ultrasonic cleaning	Stripper 104 Ultrasonic cleaning 30 min Cleaning using acetone Cleaning using IPA Check grating pattern Change the stripper solution Repeat the above process until no photoresist is left
	Au Deposition	Clean the wafer Deposit Au on the surface of the wafer	BHF Cleaning 30 sec 1st water rinse 2nd water rinse 4×10^{-3} Pa Thickness: 50 nm Deposition rate: 0.1 nm/s
	Al Deposition	Deposit Al on the backside of the wafer	4×10^{-2} Pa Thickness: 100 nm Deposition rate: 1 nm/s

Fig. A.2 Fabrication process of the Schottky photodetector with an Au grating (2/2)

Appendix B: Equipments and Chemicals Used in Fabrication Process

Table B. 1 Equipments used in fabrication process

Equipments	Provider	Type
Mask by Electron Beam Lithography Exposure	ADVANTEST Corporation	F5112+VD01
Mask Developing Equipment	EV Group	EBF101D
Compact Etcher	SAMCO	FA1
Mask Etching Equipment	FAIRCHILD	APT1140
Spin coater	MIKASA	1H-d’
Ultra High Vacuum Deposition	ULVAC	EX-400-T10
Mask Aligner	UNION KOUKI	PEM-800
Mini Vacuum Deposition	SANYU	SCV-700-2
Microscope	KEYENCE	VHX-500
Scanning Electron Microscope	HITACHI	S-4700
Atomic Force Microscope	HITACHI	SII L-trace II

Table B. 2 Chemical list used in fabrication process

Chemical Name	**Provider**	**Note**
Hydrofluoric acid	MORITA KAGAKU KOGYO	46%
OFPR800-23cp	TOKYO OHKA KOGYO CO. LTD.	Positive photoresist, 23cp
Ethanol	KANTO CHEMICAL Co., Inc	Cica-reagent grade, min 99.5%
Acetone	KANTO CHEMICAL Co., Inc	Cica-reagent grade, min 99.5%
2-Propanol	KANTO CHEMICAL Co., Inc	Cica-reagent grade, min 99.5%
NMD-3	TOKYO OHKA KOGYO CO. LTD.	TMAH 2.38%
STRIPPER104	TOKYO OHKA KOGYO CO. LTD.	Dimethyl sulfoxide 60%, N-methylpyrrolidone 40%

Appendix C: Constants Used in SPR Dip Angle Calculation

Table C. 1 Constants used in SPR dip angle calculation

Constant	symbol	Value
Speed of light in vacuum	c	299,792,458 [m/s]
Dielectric constant of air	ε_d	1
Plank constant	h	6.626068×10^{-34} m^2kg/s

Reference

[1] C. Pasquini, “Near Infrared Spectroscopy: fundamentals, practical aspects and analytical applications,” *J. Braz. Chem. Soc.*, vol. 14, no. 2, pp. 198–219, Apr. 2003.

[2] Y. Roggo, P. Chalus, L. Maurer, C. Lema-Martinez, A. Edmond, and N. Jent, “A review of near infrared spectroscopy and chemometrics in pharmaceutical technologies,” *J. Pharm. Biomed. Anal.*, vol. 44, no. 3, pp. 683–700, Jul. 2007.

[3] “a guide to NIR spectroscopic analysis of industrial manufacturing processes.pdf.” .

[4] W. Herschel, “Experiments on the Refrangibility of the Invisible Rays of the Sun. By William Herschel, LL. D. F. R. S.,” *Philos. Trans. R. Soc. Lond.*, vol. 90, no. 0, pp. 284–292, Jan. 1800.

[5] D. A. Burns and E. W. Ciurczak, *Handbook of Near-Infrared Analysis, Second Edition*. CRC Press, 2001.

[6] S. Ahuja and N. Jespersen, *Modern Instrumental Analysis*. Elsevier, 2006.

[7] I. Ben-Gera and K. H. Norris, “DETERMINATION OF MOISTURE CONTENT IN SOYBEANS BY DIRECT SPECTROPHOTOMETRY,” *Isr. J. Agric. Res.*, vol. 18, no. 3, p. 125, 1968.

[8] I. Ben-Gera and K. H. Norris, “Direct Spectrophotometric Determination of Fat and Moisture in Meat Products,” *J. Food Sci.*, vol. 33, no. 1, pp. 64–67, Jan. 1968.

[9] S. R. Delwiche, L. O. Pordesimo, A. M. Scaboo, and V. R. Pantalone, “Measurement of inorganic phosphorus in soybeans with near-infrared spectroscopy,” *J. Agric. Food Chem.*, vol. 54, no. 19, pp. 6951–6956, Sep. 2006.

[10] N. Sheibat-Othman, D. Peycelon, and G. Févotte, “Monitoring and Control of Free-Radical Polymerizations Using Near-Infrared Spectroscopy,” *Ind. Eng. Chem. Res.*, vol. 43, no. 23, pp. 7383–7391, Nov. 2004.

[11] M. Casale and R. Simonetti, “Review: Near infrared spectroscopy for analysing olive oils,” *J. Infrared Spectrosc.*, vol. 22, no. 2, pp. 59–80, 2014.

[12] M. Ferrari and V. Quaresima, “Near infrared brain and muscle oximetry: from the discovery to current applications,” *J. Infrared Spectrosc.*, vol. 20, no. 1, pp. 1–14, 2012.

[13] G. Strangman, D. A. Boas, and J. P. Sutton, “Non-invasive neuroimaging using near-infrared light,” *Biol. Psychiatry*, vol. 52, no. 7, pp. 679–693, Oct. 2002.

[14] M. Jamrogiewicz, “Application of the near-infrared spectroscopy in the pharmaceutical technology,” *J. Pharm. Biomed. Anal.*, vol. 66, pp. 1–10, Jul. 2012.

[15] D. Pérez-Marín, P. Paz, J.-E. Guerrero, A. Garrido-Varo, and M.-T. Sánchez, “Miniature handheld NIR sensor for the on-site non-destructive assessment of post-harvest quality and refrigerated storage behavior in plums,” *J. Food Eng.*, vol. 99, no. 3, pp. 294–302, Aug. 2010.

[16] E. Zamora-Rojas, D. Pérez-Marín, E. De Pedro-Sanz, J. E. Guerrero-Ginel, and A. Garrido-Varo, “In-situ Iberian pig carcass classification using a micro-electro-mechanical system (MEMS)-based near infrared (NIR) spectrometer,” *Meat Sci.*, vol. 90, no. 3, pp. 636–642, Mar. 2012.

[17] N. F. Raley et al., "A Fabry-Perot microinterferometer for visiblewavelengths," Technical Digest IEEE Solid-State Sensor and Actuator Workshop, Hilton Head Island, pp. 170-173, SC, USA, 1992.

[18] L.P. Schuler, et al., "MEMS-based microspectrometer technologies for NIR and MIR wavelengths," Journal of Physics D: Applied Physics, vol. 42, art. no. 133001, 2009.

[19] M. Blomberg, et al., "Electrically Tunable Surface Micromachined Fabry-Perot interferometer for Visible Light," Sensors and Actuators A, vol. 162, pp. 184-188, 2010.

[20] N. Neumann, M. Ebermann, K. Hiller, M. Seifert, M. Meinig, and S. Kurth, “MEMS Tunable Fabry-Pérot Filters for Infrared Microspectrometer Applications,” in *Imaging and Applied Optics 2016 (2016), paper AIT4B.2*, 2016, p. AIT4B.2.

[21] J. H. Jerman, D. J. Clift, and S. R. Mallinson, “A miniature Fabry-Perot interferometer with a corrugated silicon diaphragm support,” *Sens. Actuators Phys.*, vol. 29, no. 2, pp. 151–158, Nov. 1991.

[22] “Optical microspectrometer.” [Online]. Available: http://www.vttresearch.com. [Accessed: 07-Jun-2017].

[23] J. Antila *et al.*, “MEMS and piezo actuator-based Fabry-Perot interferometer technologies and applications at VTT,” 2010, vol. 7680, p. 76800U–76800U–12.

[24] “The Spectrometry Instrumentation & FT-IR spectroscopy With NeoSpectra,”

NeoSpectra.com. .

[25] S. H. Kong, D. D. L. Wijngaards, and R. F. Wolffenbuttel, “Infrared micro-spectrometer based on a diffraction grating,” *Sens. Actuators Phys.*, vol. 92, no. 1–3, pp. 88–95, Aug. 2001.

[26] Z. Shi, L. Fang, and C. Zhou, “Dispersive element based on grating and tunable Fabry-Perot filter in miniature spectrometer,” *Appl. Opt.*, vol. 53, no. 1, pp. 76–81, Jan. 2014.

[27] R. H. Fowler, “The analysis of photoelectric sensitivity curves for clean metals at various temperatures,” *Phys. Rev.*, vol. 38, no. 1, pp. 45–56, Jul. 1931.

[28] J. Shepherd F. D. and A. C. Yang, “Silicon Schottky retinas for infrared imaging,” in *Electron Devices Meeting, 1973 International*, 1973, vol. 19, pp. 310–313.

[29] A. Rogalski, “New Trends in Semiconductor Infrared Detectors,” *Opt. Eng.*, vol. 33, no. 5, pp. 1395–1412, May 1994.

[30] M. Kimata, T. Ozeki, N. Tsubouchi, and S. Ito, “PtSi Schottky-barrier infrared focal plane arrays,” *SPIE Milest. Ser.*, vol. 179, pp. 671–681, 2004.

[31] M. Casalino, L. Sirleto, M. Iodice, and G. Coppol, “Silicon Photodetectors Based on Internal Photoemission Effect: The Challenge of Detecting Near-Infrared Light,” in *Photodetectors*, S. Gateva, Ed. InTech, 2012.

[32] M. Casalino *et al.*, “Silicon photodetectors based on internal photoemission effect: The challenge of detecting near infrared light,” in *2014 16th International Conference on Transparent Optical Networks (ICTON)*, 2014, pp. 1–4.

[33] M. Casalino, G. Coppola, M. Iodice, I. Rendina, and L. Sirleto, “Near-Infrared Sub-Bandgap All-Silicon Photodetectors: State of the Art and Perspectives,” *Sensors*, vol. 10, no. 12, pp. 10571–10600, Nov. 2010.

[34] W. F. Kosonocky, F. V. Shallcross, T. S. Villani, and J. V. Groppe, “160 #215; 244 Element PtSi Schottky-barrier IR-CCD image sensor,” *IEEE Trans. Electron Devices*, vol. 32, no. 8, pp. 1564–1573, Aug. 1985.

[35] C. Scales and P. Berini, “Thin-Film Schottky Barrier Photodetector Models,” *IEEE J. Quantum Electron.*, vol. 46, no. 5, pp. 633–643, May 2010.

[36] M. Casalino *et al.*, “Cavity Enhanced Internal Photoemission Effect in Silicon Photodiode for Sub-Bandgap Detection,” *J. Light. Technol.*, vol. 28, no. 22, pp. 3266–3272, Nov. 2010.

[37] M. Casalino, M. Iodice, L. Sirleto, I. Rendina, and G. Coppola, “Asymmetric MSM sub-bandgap all-silicon photodetector with low dark current,” *Opt. Express*, vol. 21, no. 23, p. 28072, Nov. 2013.

[38] M. Amirmazlaghani, F. Raissi, O. Habibpour, J. Vukusic, and J. Stake, “Graphene-Si Schottky IR Detector,” *IEEE J. Quantum Electron.*, vol. 49, no. 7, pp. 589–594, Jul. 2013.

[39] *Plasmonics: Fundamentals and Applications*. Boston, MA: Springer US, 2007.

[40] W. L. Barnes, A. Dereux, and T. W. Ebbesen, “Surface plasmon subwavelength optics,” *Nature*, vol. 424, no. 6950, pp. 824–830, Aug. 2003.

[41] P. K. Jain, X. Huang, I. H. El-Sayed, and M. A. El-Sayed, “Noble Metals on the Nanoscale: Optical and Photothermal Properties and Some Applications in Imaging, Sensing, Biology, and Medicine,” *Acc. Chem. Res.*, vol. 41, no. 12, pp. 1578–1586, Dec. 2008.

[42] R. W. Wood, “On a Remarkable Case of Uneven Distribution of Light in a Diffraction Grating Spectrum,” *Proc. Phys. Soc. Lond.*, vol. 18, no. 1, p. 269, Jun. 1902.

[43] A. J. Tudos and R. B. M. Schasfoort, “Chapter 1. Introduction to Surface Plasmon Resonance,” in *Handbook of Surface Plasmon Resonance*, R. B. M. Schasfoort and A. J. Tudos, Eds. Cambridge: Royal Society of Chemistry, 2008, pp. 1–14.

[44] Lord Rayleigh, “On the Dynamical Theory of Gratings,” *Proc. R. Soc. Lond. Math. Phys. Eng. Sci.*, vol. 79, no. 532, pp. 399–416, Aug. 1907.

[45] U. Fano, “The Theory of Anomalous Diffraction Gratings and of Quasi-Stationary Waves on Metallic Surfaces (Sommerfeld’s Waves),” *J. Opt. Soc. Am.*, vol. 31, no. 3, p. 213, Mar. 1941.

[46] A. Otto, “Excitation of Nonradiative Surface Plasma Waves in Silver by Method of Frustrated Total Reflection,” *Z. Phys.*, vol. 216, no. 4, p. 398-, 1968.

[47] E. Kretschmann and H. Raether, “Radiative decay of nonradiative surface plasmons excited by light,” *Z Naturforsch A*, vol. 23, p. 2135, 1968.

[48] Y. Li, X. Liu, and Z. Lin, “Recent developments and applications of surface plasmon resonance biosensors for the detection of mycotoxins in foodstuffs,” *Food Chem.*, vol. 132, no. 3, pp. 1549–1554, Jun. 2012.

[49] S. C. B. Gopinath, “Biosensing applications of surface plasmon resonance-based Biacore technology,” *Sens. Actuators B Chem.*, vol. 150, no. 2, pp. 722–733, Oct. 2010.

[50] J. Zhang, L. Zhang, and W. Xu, “Surface plasmon polaritons: physics and applications,” *J. Phys. -Appl. Phys.*, vol. 45, no. 11, p. 113001, Mar. 2012.

[51] V. J. Sorger, R. F. Oulton, R.-M. Ma, and X. Zhang, “Toward integrated plasmonic circuits,” *Mrs Bull.*, vol. 37, no. 8, pp. 728–738, Aug. 2012.

[52] P. Berini, “Surface plasmon photodetectors and their applications,” *Laser Photonics Rev.*, vol. 8, no. 2, pp. 197–220, Mar. 2014.

[53] A. S. Karakashian, “Theory of the response of schottky-barrier diodes to transverse magnetic surface waves,” *Phys. Lett. A*, vol. 85, no. 8–9, pp. 463–466, Oct. 1981.

[54] J. Derov, Y. Y. Teng, and A. S. Karakashian, “Angular scan spectrum of a surface plasma excitation on a Schottky diode,” *Phys. Lett. A*, vol. 95, no. 3–4, pp. 197–200, Apr. 1983.

[55] A. M. Glass, P. F. Liao, D. H. Olson, and L. M. Humphrey, “Optical metal-oxide tunnel detectors with microstructured electrodes,” *Opt. Lett.*, vol. 7, no. 12, pp. 575–576, Dec. 1982.

[56] K. Berthold, W. Beinstingl, R. Berger, and E. Gornik, “Surface-Plasmon Enhanced Quantum Efficiency of Metal-Insulator-Semiconductor Junctions in the Visible,” *Appl. Phys. Lett.*, vol. 48, no. 8, pp. 526–528, Feb. 1986.

[57] S. Brueck, V. Diadiuk, T. Jones, and W. Lenth, “Enhanced Quantum Efficiency Internal Photoemission Detectors by Grating Coupling to Surface Plasma-Waves,” *Appl. Phys. Lett.*, vol. 46, no. 10, pp. 915–917, 1985.

[58] J. Hetterich, G. Bastian, N. A. Gippius, S. G. Tikhodeev, G. von Plessen, and U. Lemmer, “Optimized Design of Plasmonic MSM Photodetector,” *IEEE J. Quantum Electron.*, vol. 43, no. 10, pp. 855–859, Oct. 2007.

[59] G. Zheng, W. Zhang, L. Xu, Y. Chen, and Y. Liu, “Absorbance enhancement of thin film solar cells with front double dielectric and back metallic grating,” *Infrared Phys. Technol.*, vol. 67, pp. 52–57, Nov. 2014.

[60] M. A. Sefunc, A. K. Okyay, and H. V. Demir, “Volumetric plasmonic resonator architecture for thin-film solar cells,” *Appl. Phys. Lett.*, vol. 98, no. 9, p. 93117, Feb. 2011.

[61] M. Jestl, A. Kock, W. Beinstingl, and E. Gornik, “Polarization-Selective and Wavelength-Selective Photodetectors,” *J. Opt. Soc. Am. -Opt. Image Sci. Vis.*, vol. 5, no. 9, pp. 1581–1584, Sep. 1988.

[62] M. Jestl, I. Maran, A. Köck, W. Beinstingl, and E. Gornik, “Polarization-sensitive surface plasmon Schottky detectors,” *Opt. Lett.*, vol. 14, no. 14, p. 719, Jul. 1989.

[63] A. Sobhani *et al.*, “Narrowband photodetection in the near-infrared with a plasmon-induced hot electron device,” *Nat. Commun.*, vol. 4, p. 1643, Mar. 2013.

[64] H. Raether, *Surface plasmons on smooth and rough surfaces and on gratings*. Springer, 1988.

[65] A. F. J. Levi, *Essential Classical Mechanics for Device Physics*. IOP Publishing, 2016.

[66] Frederick Wooten, *Optical Properties of Solids*, Academic Press, 1972.

[67] A. D. Rakic, A. B. Djurišic, J. M. Elazar, and M. L. Majewski, “Optical Properties of Metallic Films for Vertical-Cavity Optoelectronic Devices,” *Appl. Opt.*, vol. 37, no. 22, p. 5271, Aug. 1998.

[68] M. J. O. (Maximilian J. O. Strutt and W. Guggenbuhl, *Semiconductor devices [by] Max J.O. Strutt*. New York: Academic Press, 1966.

[69] S. M. Sze and M.-K. Lee, *Semiconductor Devices: Physics and Technology, 3rd Edition: Physics and Technology*. John Wiley & Sons, 2012.

[70] “Frequency Selective Surface, Periodic Complementary Split Ring Resonator.” [Online]. Available: https://www.comsol.jp/model/frequency-selective-surface-periodic-complementary-split-ring-resonator-15711. [Accessed: 06-Dec-2016].

[71] “Luxpop.” [Online]. Available: http://www.luxpop.com. [Accessed: 04-Nov-2016].

[72] E. D. Palik, *Handbook of optical constants of solids*. Orlando: Academic Press, 1985.

[73] N.-F. Chiu, Y.-C. Tu, and T.-Y. Huang, "Enhanced sensitivity of anti-symmetrically structured surface plasmon resonance sensors with zinc oxide intermediate layers," *Sensors*, vol. 14, no. 1, pp. 170–187, Dec. 2013.

[74] J. Jose *et al.*, "Enhanced surface plasmon polariton propagation length using a buried metal grating," *J. Appl. Phys.*, vol. 109, no. 6, p. 64906, Mar. 2011.

[75] H. Gao, J. Henzie, M. H. Lee, and T. W. Odom, "Screening plasmonic materials using pyramidal gratings," *Proc. Natl. Acad. Sci.*, vol. 105, no. 51, pp. 20146–20151, Dec. 2008.

[76] C. Hu, "Surface plasmon resonance sensor based on diffraction grating with high sensitivity and high resolution," *Opt. - Int. J. Light Electron Opt.*, vol. 122, no. 21, pp. 1881–1884, Nov. 2011.

[77] S. K. Cheung and N. W. Cheung, "Extraction of Schottky diode parameters from forward current-voltage characteristics," *Appl. Phys. Lett.*, vol. 49, no. 2, pp. 85–87, Jul. 1986.

[78] C. Hu and D. Liu, "High-performance Grating Coupled Surface Plasmon Resonance Sensor Based on Al-Au Bimetallic Layer," *Mod. Appl. Sci.*, vol. 4, no. 6, p. 8, May 2010.

[79] M. Manley, "Near-infrared spectroscopy and hyperspectral imaging: non-destructive analysis of biological materials," *Chem. Soc. Rev.*, vol. 43, no. 24, pp. 8200–8214, 2014.

Acknowledgment

I would like to thank all the people who kindly help me during my doctoral course. It is my great honor to have Prof. Isao Shimoyama as my supervisor. I am very grateful for his all precious advices, generous encouragement and inspiration on my work. He usually explains complex thing by simple examples. Without his support, I would never complete this work. I also very appreciate Prof. Kiyoshi Matsumoto for his great advices on my work. He helped me revise my papers in great patience. I would like to thank assistant professor Tomoyuki Takahata. Whenever I ask question on optics and experimental equipment, he explains for me in details.

I would like to express my deepest grateful to assistant professor Tetsuo Kan. Without his support, I would not be able to finish this work. Before I started this work, I had very few knowledge about MEMS and barely knew surface plasmon resonance. Kan-san explained the basic mechanisms and taught me how to do the MEMS fabrication process. He gave me very generous support during my every step of research and always has great advice on how to improve my research. I also deeply appreciate all the help from Yoshiharu Ajiki-san. He gives me many great advices on semiconductor devices and always patiently explains everything from basic theory to fabrication process. I would like to express my sincerely grateful to Dr. Akihiro Isozaki. He always gave me very beneficial advices on my research and experiments. He shows me how to be a good researcher, which will benefit me in my life.

I would like to thank Dr. Hidetoshi Takahashi for his help on the fabrication of the photodetector. I also appreciate the help from Dr. Kentaro Noda to let me use his experimental equipment. I would like to thank Dr. Yasutaka Ichikawa-san, Dr. Akihito Nakai, Dr. Yusuke Takei, Dr. Nguyen Binh-Khiem and Dr. Kayoko Hirayama for their kindness and good advices on my work. I would also like to express my grateful to Dr. Takanori Usami, Dr. Nguyen Minh Dung, and Dr. Nguyen Thanh Vinh for their training of MEMS fabrication process. I also appreciate secretary Watanabe-san and Dohi-san for their help on dealing the defense procedures. I would like to thank Tsukagoshi-san and Hori-san who prepare for their doctoral defense. With their companion, I feel more

optimistic and work more productively. Thanks to my friends Koen and Sucia for the entertainments in daily life.

Finally, I would like to express my deepest gratitude to my family for their encouragement, understanding and support.

Deepest thanks to all the people around me. I wish you best luck. May you all have a wonderful life!